

# Performance and tuning of a chaotic bi-stable NES to mitigate transient vibrations

Kevin Dekemele\* · Patrick Van Torre · Mia Loccufier

Received: date / Accepted: date

**Abstract** A nonlinear energy sink (NES) passively reduces transient vibration energy of a typically impact loaded mechanical system. It is locally connected to the vibrating system through a nonlinear connecting stiffness. For a NES to perform efficiently, through targeted energy transfer (TET), the vibration levels need to exceed a well defined threshold, below which the NES performs poorly. This threshold can be lowered by considering a NES with a bi-stable connecting stiffness. A bi-stable NES (BNES) has two stable equilibria. Besides vibrating in TET regime, a BNES can also vibrate chaotically or close to one of its equilibria, called intra-well vibrations. However, during both chaotic and intra-well vibrations, the mitigating performance of the BNES is poor. Here, a novel tuning method is developed, which finds the boundary between chaotic and TET regime, such that the BNES avoids the chaos and operates with the more performant TET. This boundary is found by numerically calculating the Lyapunov exponent, a measure for chaos. To quantify performance, two algebraic expressions, requiring no simulations, are derived in the paper expressing the speed of vibration mitigation and expressing the residual vibration energy left after TET. The result is a generic tuning methodology that not only ensures the BNES operates in the efficient TET regime, but also guarantees optimal speed of vibration mitigation. The developed performances measures in function of the NES's parameters are to the point and easy to use. The tuned BNES shows a superior robustness w.r.t detuning compared to the linear vibration absorbers.


**Keywords** Passive vibration control · Nonlinear energy sink · Targeted energy transfer · Chaos

## 1 Introduction

A nonlinear energy sink (NES) is a vibration absorber, locally connected with a nonlinear stiffness to a vibrating mechanical system. It is an alternative to a linear tuned mass damper (TMD), which has linear connecting stiffness. A TMD is sensitive to a single resonating frequency, therefore a TMD is tuned to closely match the vibration frequency of the mechanical system. If this vibration frequency shifts during operation (detuning), the TMD's performance drops drastically. On the other hand, a NES has an energy-dependent resonating frequency [1,2] and as such is able to perform efficiently over a wider range of vibration frequencies. The nonlinearity of the NES makes the compound system more difficult to analyze than linear counterparts. In [1, 3, 4], the NES with cubic stiffness was analyzed through Nonlinear Normal Modes (NNMs). NNMs track the shifting resonating frequencies and steady state vibration shapes of the conservative nonlinear system for different initial energies. The behavior of the NES is divided into a low, mid and high energy regime. For low initial energy, the NES performance is abysmal. Above a clearly defined energy threshold, the NES performance vastly improves. The vibration energy is quickly transferred from the main system to the NES, where it is dissipated. This signifies the mid energy regime.

The sudden irreversible energy transfer from the vibrating system to the NES was dubbed targeted energy transfer (TET). This transient energy transfer mechanism has a few peculiarities. First, TET mitigates vibrations over a finite time while TMD damps them exponentially. Second, there will be remaining residual energy after TET which is dissipated very slowly. The residual energy is caused by transi-

---

K. Dekemele  · P. Van Torre · M. Loccufier  
Department of Electrical Energy, Metals, Mechanical Construction and Systems, Ghent University  
Tech Lane Ghent Science Park - Campus A, Technologiepark 125 & 126 B-9052 Ghent, Belgium  
E-mail: kevin.dekemele@ugent.be

tion from mid to low energy regime as the vibrations energy is reduced.

Increasing the initial energy even more gradually diminishes the performance. NMMs are obtained from the conservative system, therefore performance measures as the speed of vibration mitigation or residual energy cannot be obtained from them. In [1–6], the mitigation speed has been assessed through extensive numerical simulations of the damped compound system. This is opposite to the TMD, where the decay of the vibration is found from the poles of the compound system and is tuned by pole placement of LTI systems.

The performance of the NES is almost exclusively expressed in the percentage of initial energy dissipated in the NES, [1, 4, 5, 7–14], the complement of the residual energy. In the mentioned works it is obtained from numerical simulation. An even more important performance measure is the decay rate of the vibrations in the mechanical system, but for NESs has been given limited attention. In [10, 11], an exponential decay rate was fitted on numerical simulation to make the analogy of linear viscous damping. In [15], the time for the NES to mitigate 70 % of the initial vibration energy was determined from simulations as well. Other research investigated tuning and performance of the NES with approximate static formulas, [16, 17], where the nonlinear stiffness coefficient and damping could be analytically tuned to ensure that the NES vibrates in the performant mid-energy range. By ensuring this mid-energy regime and restricting to undamped main systems, a static algebraic formula was derived of both the duration of TET, related to the decay, called the pumping time and the residual energy after TET in [17]. The results in [17] are obtained without simulations. This point is almost never adopted in literature. In a preliminary work of the authors of this paper [18], these results were extended to other NESs and damped main systems. Here, these performance measure will be extensively applied. As the pumping time and residual energy can now be assessed without simulation, the influence of parameters as main system damping, NES damping, and other nonlinearities on NES performance can be easily analyzed. It was seen in [18] that TET performance is a balancing act between less residual energy after TET or higher decay rate during TET.

To increase the efficient energy range of the NES, a bi-stable NES (BNES) has been proposed by adding a negative linear stiffness part to connecting stiffness. It is bi-stable as it has 2 stable equilibria along with an unstable one. Here, the influence of the BNES on pumping time and residual energy will be investigated. The use of a bi-stable absorber by means of a truss was first studied in [19] and later associated with efficient TET in [12, 13]. 10 years later the BNES was put in the spotlight with a series of innovative papers [7, 14, 15, 20], where the increased efficiency range over other NESs was highlighted. In [20] the NNMs

of the compound system revealed a larger mid-energy range. Furthermore, numerical simulations shows an increased, but still suboptimal, performance in the low-energy ranges but also a possibility of a chaotic regime [15, 20, 21]. In the chaotic regime the performance of the BNES severely deteriorates. The boundary between efficient TET and chaos has to be predicted numerically on a reduced-order system [6, 14], by calculating the Lyapunov exponent from simulation. The Lyapunov exponent is a quantitative measure of chaos, defined as the average exponential growth or decay of nearby orbits near a certain initial condition. Here, the Lyapunov exponent will be employed such that the suboptimal chaotic regime is avoided. In [15] the bi-stable property is exploited such that the BNES behaves as a TMD during intra-well vibrations. This way, the residual vibration energy can be dissipated swiftly.

Recently, some papers have focussed on applications. In [8], a BNES was fitted with an electromechanical energy harvesting device. The efficiency, expressed in fraction of the impulsive energy that was harvested, was obtained from comprehensive numerical simulations. It was also found that the most energy was transferred during TET. These findings were later on experimentally verified [9]. A BNES constructed from repulsive magnets was presented in [22], and later used to reduce vibrations in multi-story structure [23].

Although great advances have been made, previous studies of the BNES focus mostly on undamped main systems, NES performance calculated after extensive and time consuming numerical simulation, and no widely applicable tuning rules are formulated. The main contributions of this paper are: 1) Developing a novel tuning methodology, applicable to a broad class of mechanical systems. The tuning will ensure operation in the TET regime and avoids the chaotic and intra-well regime. 2) Quantifying the pumping time and residual energy with 2 static algebraic expressions in function of the system's and BNES's parameters. These performance measures are also formulated for damped main systems. This way no numerical simulations are required, aiding insight in NES performance. 3) BNES parameter study on both performance and occurrence of chaotic regime, visualized on chaos - performance plots. 4) Showing the superior robustness of a BNES w.r.t. TMD under an uncertain main system and finally that 5) the vibration decay in the main system has linear pace instead of the previously assumed exponential pace during TET.

The paper is structured as follows, in the next section, the dynamics of the NES coupled to the mechanical systems are derived. In section 3 the three vibration regimes of BNES, i.e. TET, chaotic and intra-well are shown, to make the reader familiar with BNES's behavior. The dynamics of the compound system are nonlinear and therefore are simplified in section 4 with perturbation series and the two time scales technique to yield the so-called slow flow dynamics,

which reveal a slow invariant manifold. This manifold is used in section 5 to deduce the algebraic formulas expressing the performance measures pumping time and residual energy.

In section 6 the novel tuning methodology is covered, based on the calculation of the Lyapunov exponent, where the BNES coefficients are chosen as such that chaos is avoided. Then, in section 7, with tuning methodology and performances measures available, a BNES is designed for a single-mode vibrating system by constructing chaos - performance plots. Its algebraic performance is compared to other NESs, revealing superior behavior. To verify the tuning and performance, the compound system is also numerically simulated. The influence of NES damping, mass ratio and initial conditions on NES performance and the chaotic boundary is also assessed. Finally, The robustness and performance of the BNES is compared to the standard solution linear TMD, by tracking the relative change in pumping time (for BNES) and settling time (for TMD) if the vibrating frequency of the main system shifts.

## 2 System Dynamics

The considered vibrating mechanical system is a linear multi-degree-of-freedom (MDOF) system which is proportionally damped, with physical coordinate vector  $\mathbf{x} \in \mathbb{R}^n$ , mass matrix  $\mathbf{M} \in \mathbb{R}^{n \times n}$ , stiffness matrix  $\mathbf{K} \in \mathbb{R}^{n \times n}$  and damping matrix  $\mathbf{C} \in \mathbb{R}^{n \times n}$ . By solving the eigenvalue problem,  $n$  eigenfrequencies  $\omega_i$  and the eigenvector matrix,  $\mathbf{E} = [\mathbf{e}_1 \ \mathbf{e}_2 \ \dots \ \mathbf{e}_n] \in \mathbb{R}^{n \times n}$  are obtained. These allow for modal decomposition  $\mathbf{x} = \mathbf{E}\mathbf{q}$ , with  $\mathbf{q} \in \mathbb{R}^n$  the modal coordinates. Then, by attaching the BNES to coordinate  $x_\ell$ . The dynamics in modal coordinates of the compound system are:

$$\begin{cases} \mathbf{M}_q \ddot{\mathbf{q}} + \mathbf{C}_q \dot{\mathbf{q}} + \mathbf{K}_q \mathbf{q} + \mathbf{e}_*(\ell)^T (c_{na}(\dot{x}_\ell - \dot{x}_{na}) \\ \quad + k_{na}(x_\ell - x_{na})^3 + k_{lin}(x_\ell - x_{na})) = \mathbf{E}^T \mathbf{F} \\ m_{na} \ddot{x}_{na} + c_{na}(\dot{x}_{na} - \dot{x}_\ell) + k_{na}(x_{na} - x_\ell)^3 \\ \quad + k_{lin}(x_{na} - x_\ell) = 0 \end{cases} \quad (1)$$

with  $\mathbf{e}_*(\ell) \in \mathbb{R}^{n \times 1}$  the  $\ell$ -th row of  $\mathbf{E}$ ,  $\mathbf{M}_q = \mathbf{E}^T \mathbf{M} \mathbf{E}$  the modal mass,  $\mathbf{C}_q = \mathbf{E}^T \mathbf{C} \mathbf{E}$  the modal damping and  $\mathbf{K}_q = \mathbf{E}^T \mathbf{K} \mathbf{E}$  the modal stiffness matrix. The NES behaves as a BNES for  $k_{lin} < 0$ . The connecting force of the NES on the main system can be replaced by its inertia force:

$$\begin{cases} \mathbf{M}_q \ddot{\mathbf{q}} + \mathbf{C}_q \dot{\mathbf{q}} + \mathbf{K}_q \mathbf{q} + \mathbf{e}_*(\ell)^T m_{na} \ddot{x}_{na} = \mathbf{E}^T \mathbf{F} \\ m_{na} \ddot{x}_{na} + c_{na}(\dot{x}_{na} - \dot{x}_\ell) + k_{na}(x_{na} - x_\ell)^3 \\ \quad + k_{lin}(x_{na} - x_\ell) = 0 \end{cases} \quad (2)$$

The equations are simplified by assuming a single vibration mode  $i$ :  $\mathbf{x}(t) =$

$\sum_{k=1}^n \mathbf{e}_k q_k(t) = \mathbf{e}_i q_i(t)$  and only considering transient vibrations,  $\mathbf{F} = \mathbf{0}^{n \times 1}$ . The physical coordinate  $x_\ell = e_i(\ell) q_i$  is reintroduced:

$$\begin{cases} \frac{m_{q,i}}{e_i(\ell)} \ddot{x}_\ell + \frac{c_{q,i}}{e_i(\ell)} \dot{x}_\ell + \frac{k_{q,i}}{e_i(\ell)} x_\ell + m_{na} e_i(\ell) \ddot{x}_{na} = 0 \\ \varepsilon \ddot{x}_{na} + \varepsilon \lambda_{na} (\dot{x}_{na} - \dot{x}_\ell) + \varepsilon \Omega_3 \omega_i^4 (x_{na} - x_\ell)^3 \\ \quad + \varepsilon \kappa \omega_i^2 (x_{na} - x_\ell) = 0 \end{cases} \quad (3)$$

with  $m_{q,i} = M_q(i, i)$ ,  $k_{q,i} = K_q(i, i)$  and  $c_{q,i} = C_q(i, i)$ . The  $n+1$  DOF problem is reduced to a 2DOF problem, depicted on Figure 1.

Dividing the first equation by  $e_i(\ell)$  yields:

$$\begin{cases} \ddot{x}_\ell + \varepsilon \lambda \dot{x}_\ell + \omega_i^2 x_\ell + \varepsilon \ddot{x}_{na} = 0 \\ \varepsilon \ddot{x}_{na} + \varepsilon \lambda_{na} (\dot{x}_{na} - \dot{x}_\ell) + \varepsilon \Omega_3 \omega_i^4 (x_{na} - x_\ell)^3 \\ \quad + \varepsilon \kappa \omega_i^2 (x_{na} - x_\ell) = 0 \end{cases} \quad (4)$$

with

$$\begin{aligned} \varepsilon \lambda &= \frac{c_{q,i}}{m_{q,i}} & \omega_i^2 &= \frac{k_{q,i}}{m_{q,i}} & \varepsilon &= \frac{m_{na} e_i^2(\ell)}{m_{q,i}} \\ \kappa &= \frac{k_{lin}}{m_{na} \omega_i^2} & \lambda_{na} &= \frac{c_{na}}{m_{na}} & \Omega_3 &= \frac{k_{na}}{m_{na} \omega_i^4} \end{aligned}$$

Although (4) is derived from an MDOF main system, it is also valid for an SDOF main system with mass  $m$ , damping  $c$  and stiffness  $k$  equipped with a BNES granted if  $m_{q,i} = m$ ,  $k_{q,i} = k$ ,  $c_{q,i} = c$  and  $e_i(\ell) = 1$ .

For  $\kappa < 0$ , the system has 3 equilibrium points. Through linearization it can be shown that first one,  $x^{*,1} = \{x_{\ell,1}^*, x_{na,1}^*\} = \{0, 0\}$ , is unstable, while the other two  $x^{*,2,3} = \{x_{\ell}^{*,2,3}, x_{na}^{*,2,3}\} = \{0, \pm \frac{1}{\omega_i} \sqrt{\frac{-\kappa}{\Omega_3}}\}$  are stable. To describe small vibrations about both stable equilibria, the so-called the intra-well vibrations, (4) is linearized about  $x^{*,2,3}$ :

$$\begin{cases} \Delta \ddot{x}_\ell + \varepsilon \lambda \Delta \dot{x}_\ell + \omega_i^2 \Delta x_\ell + \varepsilon \Delta \ddot{x}_{na} = 0 \\ \varepsilon \Delta \ddot{x}_{na} + \varepsilon \lambda_{na} (\Delta \dot{x}_{na} - \Delta \dot{x}_\ell) + 2\varepsilon \kappa \omega_i^2 (\Delta x_{na} - \Delta x_\ell) = 0 \end{cases} \quad (5)$$

where the nonlinear coefficient  $k_{na}$  has completely disappeared. If in (5)  $\kappa = -0.5$ , the BNES acts as a linear TMD, as the linearized eigenfrequency of the absorber equals the vibration frequency of the vibrating structure. The absorber performance for  $\kappa = -0.5$  will be compared to others choices of  $\kappa$  further on. The nonlinear differential equation in (4) does not have an exact analytical solution. Therefore, semi-analytic techniques will be applied in Section 4 which will result an approximate solution on a slow time scale.

Next, the characteristic vibration regimes of the BNES are shown.

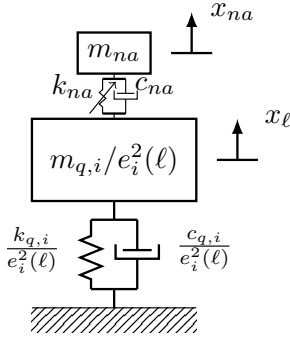


Fig. 1: The equivalent 2DOF, (4), deduced from single-mode vibrating mechanical systems fitted with a NES

### 3 Vibration regimes of a BNES

A single-degree-of-freedom mechanical system with  $m = 1$  kg,  $k = 1$  N/m,  $c = 0.002$  Ns/m and coordinate  $x$  features a BNES with  $m_{na} = 0.02$  kg,  $k_{lin} = -0.006$  N/m,  $c_{na} = 0.002$  Ns/m,  $k_{na} = 0.444$  N/m<sup>3</sup> and coordinate  $x_{na}$ .

For  $\dot{x}(0) = 0.1$  m/s, TET occurs, with Figure 2a the main system's vibrations and Figure 2d the relative NES coordinate  $x - x_{na}$ . During TET, the energy from the main vibrating system is transferred to the BNES, where it is dissipated. The energy transfer is suddenly halted (after the pumping time) while a small fraction of the vibration energy remains (the residual energy). This behavior is identical to TET for a NES without bi-stable property,  $k_{lin} \geq 0$ . However, there are two unique ways the BNES vibrates, called the chaotic inter-well vibrations and the intra-well vibrations as shown in [14].

When the initial velocity is lowered to  $\dot{x}(0) = 0.05 \frac{m}{s}$ , the BNES vibrates chaotically, Figure 2e. Figure 2b illustrates that vibration energy in the main mass reduces much slower than before. Finally, for the even lower  $\dot{x}(0) = 0.01 \frac{m}{s}$ , the BNES is not capable of leaving its *well*, Figure 2f, as the BNES does not vibrate around its zero position. Again the vibration energy in the main system is reduced rather slowly, Figure 2c. Later on, a tuning methodology for the BNES will be proposed to ensure it operates in the efficient TET region and avoids the lower energy chaotic and intra-well behavior. A glance at the stiffness force  $F(x) = k_{na}v^3$ ,  $F(x) = k_{lin}v + k_{na}v^3$  and potential energy  $V(x) = k_{na} \frac{v^4}{4}$ ,  $V(x) = k_{lin} \frac{v^2}{2} + k_{na} \frac{v^4}{4}$  of either the purely cubic and bi-stable stiffness clarifies their similarities and differences, with  $v = x_{na} - x$ ,  $k_{na} = 0.444$  N/m<sup>3</sup> and  $k_{lin} = -0.006$  N/m. For high relative displacement, Figure 3a and 3c, both the force and potential energy are almost identical, which explains why their behavior is also similar (TET) for both  $k_{lin} \geq 0$  and  $k_{lin} < 0$ . For smaller relative displacement, both the force

and potential are drastically different. On the force characteristic, Figure 3b, the sign of the force and displacement of the BNES is different for  $v \in [-\sqrt{\frac{-k_{lin}}{k_{na}}}, \sqrt{\frac{-k_{lin}}{k_{na}}}]$ . This reflects in the potential in Figure 3d as a negative potential energy and two minima at  $v = \{-\sqrt{\frac{-k_{lin}}{k_{na}}}, \sqrt{\frac{-k_{lin}}{k_{na}}}\}$  which form the so-called *wells*. Inter-well vibrations are vibrations around the zero-position while intra-well vibrations happen in one of the wells around a non-zero equilibria. For these lower energies, the inter-well chaotic and the intra-well vibration occur only for the BNES.

## 4 Approximate dynamics and tuning

### 4.1 Semi-analytic reduction

In this section the nonlinear dynamics of (4) are simplified by deriving the slow flow dynamics and a slow invariant manifold (SIM). The result will help us define several *algebraic* performance measures for targeted energy transfer obtained. They are called algebraic as these are found without simulation of the dynamic system (1)

Although this paper focusses on the BNES, the calculations in this section are also valid for  $\kappa \geq 0$ .

New variables are introduced,  $u = x_l + \varepsilon x_{na}$ , the center of mass of modal/absorber system (4), and  $v = x_l - x_{na}$ , the relative absorber movement. Rewriting (4) in these new variables yields:

$$\begin{cases} \ddot{u} + \omega_i^2 u + \varepsilon (\lambda \dot{u} + \omega_i^2 (v - u)) + \mathcal{O}(\varepsilon^2) = 0 \\ \varepsilon (\ddot{v} + \omega_i^2 v) + \varepsilon \omega_i^2 (u - v) + \varepsilon \lambda_{na} \dot{v} + \varepsilon \omega_i^4 \Omega_3 v^3 \\ \quad + \varepsilon \kappa \omega_i^2 v + \mathcal{O}(\varepsilon^2) = 0 \end{cases} \quad (6)$$

where a small mass ratio  $\varepsilon \ll 1$  is assumed such that the terms  $\mathcal{O}(\varepsilon^2)$  can be omitted and  $\varepsilon \ddot{u} \approx -\varepsilon \omega_i^2 u$ .

Variables  $u$  and  $v$  are assumed to vibrate with a single mode, 1:1 resonance, so they can be complexified to:

$$\begin{cases} \varphi(t) e^{j\omega_i t} = \dot{u} + j\omega_i u, \varphi \in \mathbb{C} \\ \varphi_{na}(t) e^{j\omega_i t} = \dot{v} + j\omega_i v, \varphi_{na} \in \mathbb{C} \end{cases} \quad (7)$$

with  $j = \sqrt{-1}$  the imaginary unit and with both  $\varphi(t)$  and  $\varphi_{na}(t)$  modulating the amplitude and phase and  $e^{j\omega_i t}$  an oscillation with frequency  $\omega_i$  in the complex plane. This allows for a change of variables in the complexified variables:

$$\begin{cases} u = \frac{\varphi e^{j\omega_i t} - \bar{\varphi} e^{-j\omega_i t}}{2j\omega_i} & v = \frac{\varphi_{na} e^{j\omega_i t} - \bar{\varphi}_{na} e^{-j\omega_i t}}{2j\omega_i} \\ \dot{u} = \frac{\varphi e^{j\omega_i t} + \bar{\varphi} e^{-j\omega_i t}}{2} & \dot{v} = \frac{\varphi_{na} e^{j\omega_i t} + \bar{\varphi}_{na} e^{-j\omega_i t}}{2} \\ \ddot{u} + \omega_i^2 u = \dot{\varphi} e^{j\omega_i t} & \ddot{v} + \omega_i^2 v = \dot{\varphi}_{na} e^{j\omega_i t} \end{cases} \quad (8)$$

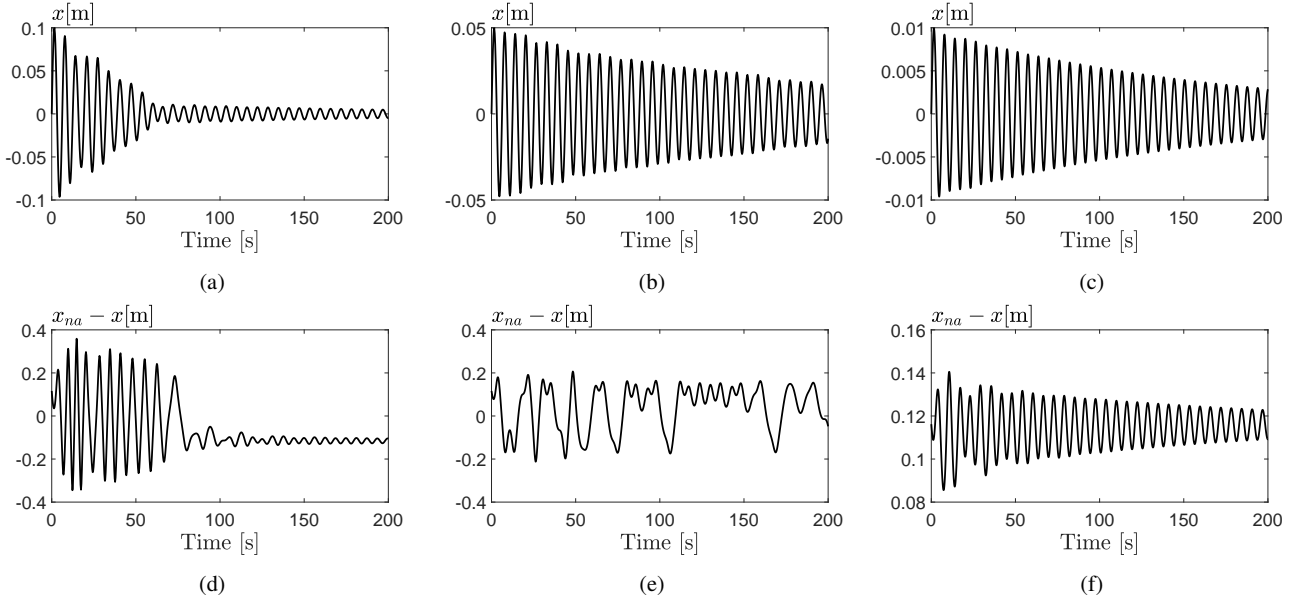


Fig. 2: Numerical simulation for  $\dot{x}(0) = 0.1$ , main system (a) and BNES (d) vibration, and chaotic vibrations for  $\dot{x}(0) = 0.05$ , main system (b) and BNES (e), and intra-well for  $\dot{x}(0) = 0.01$ , main system (c) and BNES (f)

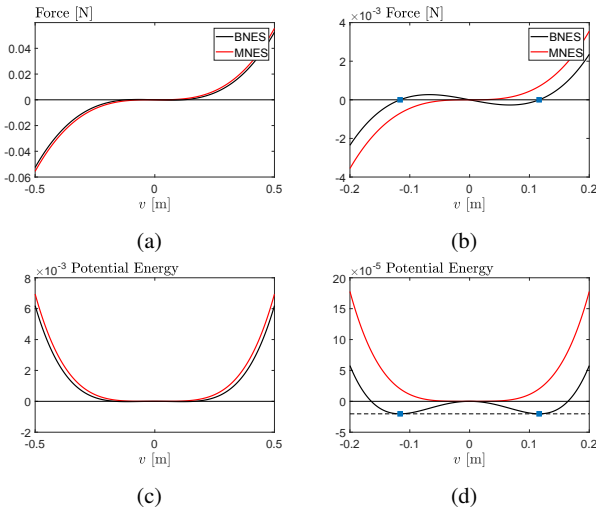


Fig. 3: Force characteristic of NES and BNES for low (a) and high (b) relative displacement and potential energy low (c) and high (d) relative displacement.

with the bar sign the complex conjugate. The complexified variables are expanded in a perturbation series:

$$\begin{cases} \varphi = \varphi_0 + \varepsilon\varphi_1 + \varepsilon^2\varphi_2 + \dots \\ \varphi_{na} = \varphi_{na0} + \varepsilon\varphi_{na1} + \varepsilon^2\varphi_{na2} + \dots \end{cases} \quad (9)$$

which expands the variable  $\varphi$  (and  $\varphi_{na}$ ) into a sum of terms with decreasing importance,  $\varepsilon^i\varphi_i$  ( $\varepsilon^i\varphi_{nai}$ ). The perturbation series here is taken up to a first order power  $\varepsilon$ , while  $\mathcal{O}(\varepsilon^2)$  and higher considered insignificant. This way, both

$\varphi$  and  $\varphi_{na}$  only consist of a major ( $\mathcal{O}(\varepsilon^0)$ ), denoted by index 0 and a minor ( $\mathcal{O}(\varepsilon^1)$ ) contribution, denoted by index 1. A perturbation series often yields a bad approximation of the actual dynamics on a long time scale. Therefore, the perturbation series is often combined with the two-timing technique, which assumes that the dynamics act on two separate and independent time variables (hence two-timing), a fast  $T_0 = t$  and a slow  $T_1 = \varepsilon t$  time. Although both time scales are not independent, in two-timing it is assumed they are. Then, the derivative w.r.t.  $t$  is a total derivative up to  $\mathcal{O}(\varepsilon)$ :

$$\frac{d}{dt} = \frac{\partial}{\partial T_0} + \varepsilon \frac{\partial}{\partial T_1} \quad (10)$$

Two-timing will ensure that the reduced dynamics of the perturbation series approximate the real dynamics on short and on long term. Applying the complexification, the perturbation and two-timing on (6) and neglecting terms  $\mathcal{O}(\varepsilon^2)$  and beyond:

$$\begin{cases} \frac{\partial \varphi_0}{\partial T_0} + \varepsilon \frac{\partial \varphi_0}{\partial T_1} + \varepsilon \frac{\partial \varphi_1}{\partial T_0} + \varepsilon \lambda \frac{\varphi_0}{2} + \varepsilon \frac{\omega_i^2}{2j\omega_i} (\varphi_{na0} - \varphi_0) \\ + \left( \varepsilon \lambda \frac{\bar{\varphi}_0}{2} - \varepsilon \frac{\omega_i^2}{2j\omega_i} (\bar{\varphi}_{na0} - \bar{\varphi}_0) \right) e^{-2j\omega_i t} = 0 \\ \varepsilon \left( \frac{\partial \varphi_{na0}}{\partial T_0} \right) + \varepsilon \frac{\omega_i^2}{2j\omega_i} (\varphi_0 - \varphi_{na0}) + \varepsilon \lambda_{na} \frac{\varphi_{na0}}{2} + \frac{\varepsilon \kappa \omega_i^2}{2j\omega_i} \varphi_{na0} \\ + \left( -\varepsilon \frac{\omega_i^2}{2j\omega_i} (\bar{\varphi}_0 - \bar{\varphi}_{na0}) + \varepsilon \lambda_{na} \frac{\bar{\varphi}_{na0}}{2} - \frac{\varepsilon \kappa \omega_i^2}{2j\omega_i} \bar{\varphi}_{na0} \right) e^{-2j\omega_i t} \\ + \frac{\varepsilon \omega_i^4 \Omega_3}{8(j\omega_i)^3} \sum_{k=0}^3 (-1)^k \binom{3}{k} \varphi_{na}^{3-k} \bar{\varphi}_{na}^k e^{j(3-2k-1)\omega_i t} = 0 \end{cases}$$

(11)

Both equations of (11) show terms with higher order harmonics. These terms may result in unbounded solutions and are referred to as secular terms. We omit all secular terms, a characteristic manipulation of two-timing [24]:

$$\begin{cases} \frac{\partial \varphi_0}{\partial T_0} + \varepsilon \frac{\partial \varphi_0}{\partial T_1} + \varepsilon \frac{\partial \varphi_1}{\partial T_0} + \varepsilon \lambda \frac{\varphi_0}{2} + \varepsilon \frac{\omega_i^2}{2j\omega_i} (\varphi_{na0} - \varphi_0) = 0 \\ \varepsilon \left( \frac{\partial \varphi_{na0}}{\partial T_0} \right) + \varepsilon \frac{\omega_i^2}{2j\omega_i} (\varphi_0 - \varphi_{na0}) + \varepsilon \lambda_{na} \frac{\varphi_{na0}}{2} + \frac{\varepsilon \kappa \omega_i^2}{2j\omega_i} \varphi_{na0} \\ - \varepsilon \frac{j\omega_i^4 \Omega_3}{8\omega_i^3} 3|\varphi_{na0}|^2 \varphi_{na0} = 0 \end{cases} \quad (12)$$

The same result would have been obtained if the averaging technique is performed [1]. The next step in our procedure consists in equating the coefficients of  $\varepsilon^0$  and  $\varepsilon$ :

$$\begin{cases} \frac{\partial \varphi_0}{\partial T_0} = 0 \Rightarrow \varphi_0(T_1) \\ \frac{\partial \varphi_0}{\partial T_1} + \frac{\partial \varphi_1}{\partial T_0} + \frac{\lambda \varphi_0}{2} + \frac{\omega_i^2 \varphi_{na0}}{2j\omega_i} - \frac{\omega_i^2 \varphi_0}{2j\omega_i} = 0 \\ \frac{\partial \varphi_{na0}}{\partial T_0} + \frac{\lambda_{na} \varphi_{na0}}{2} + \frac{\omega_i^2 \varphi_0}{2j\omega_i} - \frac{\omega_i^2 (1 - \kappa) \varphi_{na0}}{2j\omega_i} \\ - j \frac{3\Omega_3 \omega_i^4}{8\omega_i^3} |\varphi_{na0}|^2 \varphi_{na0} = 0 \end{cases} \quad (13)$$

The first equation of (13) states that  $\varphi_0$  is constant on a fast time scale  $T_0$ , only evolving on the long term ( $T_1$ ) according to the other equations. It can be shown [25] that both  $\varphi_{na0}$  and  $\varphi_1$  evolve towards a steady state as  $T_0 \rightarrow \infty$ ;  $\lim_{T_0 \rightarrow \infty} \varphi_{na0} = \Phi_{na0}$  and  $\lim_{T_0 \rightarrow \infty} \varphi_1 = \Phi_1$ ; This way, (13) can be described in steady state for  $T_0$ , solely behaving on the slow time scale  $T_1$

$$\begin{cases} \frac{\partial \varphi_0}{\omega_i \partial T_1} = -\frac{\xi \varphi_0}{2} + \frac{j\Phi_{na0}}{2} - \frac{j\varphi_0}{2} \\ 0 = -\frac{j(1 - \kappa) + \xi_{na}}{2} \Phi_{na0} + \frac{j\varphi_0}{2} + \frac{3j\Omega_3}{8} (|\Phi_{na0}|^2 \Phi_{na0}) \end{cases} \quad (14)$$

with  $\xi = \frac{\lambda}{\omega_i}$  and  $\xi_{na} = \frac{\lambda_{na}}{\omega_i}$  dimensionless damping parameters.

(14) describes the dynamics of only the major contributions of the perturbation series (9) ( $\varphi_0$  and  $\varphi_{na0}$ ). These major contributions are assumed to be representative of the actual dynamics, which later on will be verified through numerical simulation. The complexified variables are written

in polar notation;  $\varphi_0(T_1) = R_0(T_1)e^{j\delta_0(T_1)}$  and  $\Phi_{na0}(T_1) = R_{na}(T_1)e^{j\delta_{na}(T_1)}$  with  $R_0, R_{na}, \delta_0$  and  $\delta_{na} \in \mathbb{R}$ .  $R_0$  and  $R_{na}$  are the amplitude modulating part (the envelope). Then splitting (14) in real and imaginary parts yields after some calculations:

$$\begin{cases} \frac{1}{\omega_i} \frac{\partial R_0}{\partial T_1} = -\frac{\xi R_0}{2} - \frac{\sin(\delta_{na} - \delta_0)}{2} R_{na} \\ \frac{R_0}{\omega_i} \frac{\partial \delta_0}{\partial T_1} = -\frac{R_0}{2} + \frac{\cos(\delta_{na} - \delta_0)}{2} R_{na} \\ 0 = -\frac{\sin(\delta_0 - \delta_{na})}{2} R_0 - \frac{\xi_{na}}{2} R_{na} \\ 0 = \frac{\cos(\delta_0 - \delta_{na})}{2} R_0 - \frac{1 - \kappa}{2} R_{na} + \frac{3\Omega_3}{8} R_{na}^3 \end{cases} \quad (15)$$

The equation (15) is manipulated as follows. The squared sum of the third and fourth equation yield a static relationship between  $R_0$  and  $R_{na}$ , while a substitution of the third in the first equation simplifies the slow time dynamic equation:

$$\begin{cases} \frac{1}{\omega_i} \frac{\partial R_0^2}{\partial T_1} = -\xi R_0^2 - \xi_{na} R_{na}^2 \\ R_0^2 = \left[ \xi_{na}^2 + \left( 1 - \kappa - \frac{3\Omega_3}{4} R_{na}^2 \right)^2 \right] R_{na}^2 \end{cases} \quad (16)$$

The energy-like variables  $E_0 = R_0^2 \in \mathbb{R}_+$  and  $E_{na} = R_{na}^2 \in \mathbb{R}_+$  are introduced along with their dimensionless counterparts  $Z_0 = \Omega_3 E_0$  and  $Z_{na} = \Omega_3 E_{na}$ . Then (16) becomes:

$$\begin{cases} \frac{\partial Z_0}{\partial T_1} = -\lambda Z_0 - \lambda_{na} Z_{na} \\ Z_0 = \left[ \xi_{na}^2 + \left( 1 - \kappa - \frac{3}{4} Z_{na} \right)^2 \right] Z_{na} \end{cases} \quad (17)$$

(17) represents the slow flow dynamics. The first equation states that  $Z_0$ , the dimensionless energy in the center of mass, always decreases in time. The second equation is a *slow invariant manifold* (SIM), which restricts the relation between  $Z_0$  and  $Z_{na}$  on the phase plane. The SIM is plotted for a combination  $\xi_{na}$ 's and  $\kappa$ 's on Figure 4a and Figure 4b. Notice that there is a region where 3 solutions of  $Z_{na}$  exist for one  $Z_0$ . Next, the importance of the SIM in tuning and performance is discussed and related to these 3 branches.

## 4.2 Analysis of SIM

### 4.2.1 Multiple branches and conditions for TET

The points of interest on the SIM are its extrema:

$$\begin{cases} Z_{na\pm} = \frac{4}{9} \left( 2(1 - \kappa) \pm \sqrt{(1 - \kappa)^2 - 3\xi_{na}^2} \right) \\ Z_0^\pm = \left[ \xi_{na}^2 + \left( 1 - \kappa - \frac{3}{4} Z_{na\mp} \right)^2 \right] Z_{na\mp} \end{cases} \quad (18)$$

with  $\{Z_0^+, Z_{na}^-\}$  a local maximum and  $\{Z_0^-, Z_{na}^+\}$  a local minimum which exist for

$$\xi_{na} < \frac{1 - \kappa}{\sqrt{3}} \quad (19)$$

Depending on where the dynamics initiate on the SIM, the ability of the NES in mitigating vibrations differs. On the right branch,  $Z_0 > Z_0^-$  and  $Z_{na} > Z_{na}^+$ ,  $Z_{na}$  is large meaning that  $\frac{\partial Z_0}{\partial T_1}$  is large and negative as well, (17). This fast decrease of vibration energy in  $Z_0$  is TET. The right branch is descended until the point  $\{Z_{na}^+, Z_0^-\}$ , see Figure 4c. At this point, the SIM can not be ascended as  $Z_0$  should always decrease. The dynamics will then jump to the left branch, where  $Z_{na}$  is small. On this branch  $\frac{\partial Z_0}{\partial T_1}$  is small as well, with the residual vibration energy  $Z_0^-$  only gradually decreasing. To conclude, the condition for TET, is to initiate on the right branch of the SIM. The performance can also be derived from the SIM. The pumping time is the duration of the descent on the right branch up until the local minimum  $\{Z_{na}^+, Z_0^-\}$ . The residual energy is what is left after TET, namely  $Z_0^-$ . These two measures are essential for TET performance. It can already be seen on Fig. 4a, increasing the damping will increase the residual energy, as  $Z_0^-$  is higher.

### 4.2.2 Initial conditions and SIM

To ensure that TET is triggered, the SIM and its relation to initial conditions of  $v$  and  $u$  of (6) needs to be understood. As these initial conditions can be chosen arbitrarily, the dynamics can initiate anywhere on the  $Z_{na}Z_0$ -plane, not necessarily on the SIM. Since the SIM described the dynamics on the slow time scale, the actual dynamics on the fast time still need to converge from the initial point to the SIM.

Only impulsive excitation will be investigated, where the main system is only subjected to an initial speed,  $\dot{x}_\ell(0) \neq 0$ ,  $x_\ell(0) = \dot{x}_{na}(0) = 0$  then  $\dot{u} = \dot{v} = \dot{x}_\ell(0)$ . For  $\kappa < 0$ , there is also an initial displacement for the BNES as it rests in one of the stable positions,  $u(0) = -\frac{\varepsilon}{\omega_i} \sqrt{\frac{-\kappa}{\Omega_3}}$  and  $v(0) = \frac{1}{\omega_i} \sqrt{\frac{-\kappa}{\Omega_3}}$ . With  $Z_0(0) = \Omega_3(\dot{u}_0^2(0) + \omega_i^2 u_0^2(0))$  and  $Z_{na}(0) = \Omega(\dot{v}_0^2(0) + \omega_i^2 v_0^2(0))$ , an impulsive excitation will initiate on the  $Z_{na} - Z_0$  phase plane on:

- The line through the origin  $Z_0 = Z_{na}$  for  $\kappa \geq 0$
- The line  $Z_0 = Z_{na} + (1 - \varepsilon)\kappa$  for  $\kappa < 0$

These lines of initial points are drawn together with the SIM on Fig.4c and Fig.4d for  $\kappa = 0$  and Fig.4e and Fig.4f for  $\kappa = -0.5$ . When  $Z_0(0) > Z_0^+$  on Fig. 4c and Fig. 4e, there is only one corresponding  $Z_{na}$  on the SIM. In this case the dynamics will converge to the right branch. This condition for TET has been found in previous works as well, and is confirmed with numerical simulations of (1) [16–18].

For  $Z_0^- < Z_0(0) < Z_0^+$ , there are three solutions in  $Z_{na}$ , on the suboptimal left branch, on the unstable middle branch [25] and on the optimal right branch. **For  $\kappa = 0$ , the line of initial points will be very close to the left branch, Fig.4d. Therefore, the dynamics are very likely attracted to this slow, sub-optimal branch, confirmed by simulations in [16, 17]. For  $\kappa \geq 0$ ,  $Z_0(0) > Z_0^+$  is thus the energy threshold above which TET is triggered.** A NES with  $\kappa \geq 0$  can thus be tuned as follows:

$$Z_0(0) > Z_0^+ \rightarrow k_{na} \geq \frac{m_{na}\omega_i^4(Z_0^+)}{\dot{u}^2(0) + \omega_i^2 u^2(0)} \quad (20)$$

When a BNES is considered,  $\kappa < 0$ , Fig.4f, the branch convergence is more ambiguous. The initial line is now to the right of the suboptimal branch, and intersects with the unstable branch. As the initial points are not close to either of the stable branches, is it uncertain whether the dynamics are attracted to the left or right branch for  $Z_0^- < Z_0(0) < Z_0^+$  when  $\kappa < 0$ , visualized by the red dash and blue dotted lines on Fig.4f. In Section 6 it will be shown that there is an energy threshold lower than  $Z_0^+$  for  $\kappa < 0$ , below which the BNES vibrates chaotically. The range for TET is thus extended for the BNES. Numerical simulations of (1) in Section 7.1 will confirm this. In Section 3, the simulated system with BNES has a  $Z_0^+ = 0.4217$ . For  $\dot{x}(0) = 0.1$ , there is TET even though  $Z(0) = 0.2222$ , confirming that TET is also possible for  $Z_0^- < Z_0(0) < Z_0^+$  when  $\kappa < 0$ .

Essential for tuning and performance is the knowledge of  $Z_0(0)$ . It can be difficult to obtain with certainty the initial conditions from impact loaded systems. If a range of initial energies is available,  $[Z_{0,min}(0), Z_{0,max}(0)]$ , only  $Z_{0,min}(0)$  needs to be considered in tuning to ensure TET for the whole energy range. In practical applications, initials speeds can be derived from the intensity of impact or shock forces.

## 5 Performance measures

The performance of the NES in mitigating transient vibrations is either expressed in the amount of energy dissipation during TET (and the complementary residual energy) or speed or decay of this dissipation. The latter is often overlooked and the NES performance is only expressed in the energy dissipation, calculated from numerical simulations.

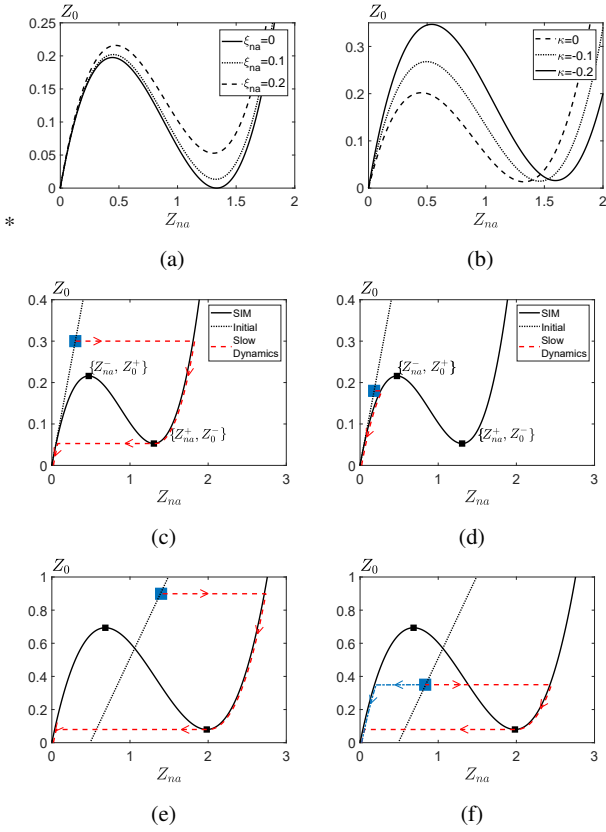


Fig. 4: The SIM for  $\kappa = 0$  and  $\xi_{na} = [0, 0.1, 0.2]$  (a),  $\kappa = [0, -0.1, -0.2]$  and  $\xi_{na} = 0.1$  (b). Attraction to right branch for  $\kappa = 0$  and  $\xi_{na} = 0.1$  (c) and  $\kappa = -0.5$  and  $\xi_{na} = 0.1$  (d), with black-dotted line of possible starting points, blue square dot the starting point and red the dynamics in slow flow. Reducing the initial energy causes attraction to the left branch for  $\kappa = 0$  and  $\xi_{na} = 0.1$  by reducing initial energy (e) but  $\kappa = -0.5$  it is unclear which branch is taken (f).

Extensive numerical simulations are thus required to gain insight and optimize performance. The performance measures introduced in this section do not require simulations to calculate, but only the parameters of the mechanical system and NES. To introduce the concept of the performance measures proposed in this paper, the slow flow dynamics (17) are numerically integrated for  $\xi_{na} = 0.1$  and  $\kappa = 0$ . Once for  $Z_0(0) = 0.22$  and starting on the right branch, similar to Fig 4c, and once for  $Z_0(0) = 0.2$  starting on the left branch, similar to Fig 4d. The corresponding time evolution of  $Z_0$  and  $Z_{na}$  in slow time are shown on Fig. 5. For  $Z_0(0) = 0.22$ ,  $Z_0$  (red) decreases swiftly until the slope suddenly changes. The corresponding  $Z_{na}$  (red) has a high value and decreases slowly until it jumps to a very low value, at the same time the slope of  $Z_0$  changes. The time of efficient energy transfer is called pumping time. After the slope change of  $Z_0$ , there is some residual energy left ( $Z_0^-$ ). For  $Z(0) = 0.20$ ,  $Z_0$  (black) decreases at sluggish pace while  $Z_{na}$  has a very low value.

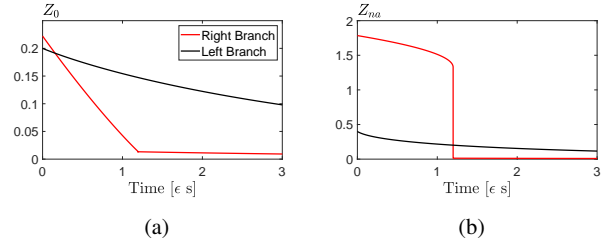


Fig. 5: Slow flow dynamics time evolution for  $\kappa = 0$  and  $\xi_{na} = 0.1$  with  $Z_0(0) = 0.22$  (red) and  $Z_0(0) = 0.2$  (black) .

It is now the goal of this section to determine the pumping time and residual energy based on static formulas, instead of numerical simulations of (17). These are the algebraic performance measures, called like this to stress no differential equation needs to be solved to obtain the pumping time and residual energy.

The decay of  $Z_0$  of Figure 4c is more linear rather than exponential, the latter typical in linear systems. This is because during TET,  $Z_{na}$  is nearly constant, such that according to the first equation of (17) the decrease of  $Z_0$  is nearly constant. However, in some works [10, 11] the exponential decay  $e^{-\zeta\omega t}$  was incorrectly fitted on simulations where  $\zeta$  is then a measure for TET speed.

For this algebraic performance to match the actual performance, the slow flow dynamics should be representative of the actual dynamics, which will be verified in Section 7.1.

### 5.1 Residual Energy and Energy dissipation

If the slow dynamics initiate on the right branch of the SIM, TET persist until the local minimum of the SIM, Figure 4c. The residual energy relative to the initial energy is then:

$$E_{res} = \frac{Z_0^-}{Z_0(0)} = \frac{E_0^-}{E_0(0)} \quad (21)$$

with its complement the fraction of the initial energy dissipated by the NES during TET:

$$E_{TET} = 1 - \frac{Z_0^-}{Z_0(0)} = 1 - \frac{E_0^-}{E_0(0)} \quad (22)$$

and is dubbed the energy dissipation [17]. These measures can also be expressed in amplitude:

$$A_{res} = \frac{\sqrt{Z_0^-}}{\sqrt{Z_0(0)}} \quad A_{TET} = 1 - \frac{\sqrt{Z_0^-}}{\sqrt{Z_0(0)}} \quad (23)$$

As  $Z_0(0) = \Omega_3(\dot{u}(0)^2 + \omega_t^2 u^2(0))$  and  $Z_0^-$  is (18), both (21) and (22) can be calculated without any numerical integration of (17). In literature, the fraction of the initial energy dissipated by the NES is the most common way to express the NES performance. Now it is expressed in a simple



formula (22) instead of determined from numerical simulations.

### 5.2 Pumping time of undamped main system

From (17), the derivate of  $Z_{na}$  w.r.t.  $T_1$  is:

$$\frac{1}{\omega_i} \frac{\partial Z_{na}}{\partial T_1} = \frac{-\xi_{na} Z_{na} - \xi Z_0}{\frac{27}{32} Z_{na}^2 - 3(1-\kappa) Z_{na} + (1-\kappa)^2 + \xi_{na}^2} \quad (24)$$

If there is no damping in the main system,  $\xi = 0$ , separation of variables  $Z_{na}$  and  $T_1$  is possible, which after integration results in:

$$\overbrace{\frac{27}{16} Z_{na}^2 - 3Z_{na}(1-\kappa) + \left( (1-\kappa)^2 + \xi_{na}^2 \right) \ln(Z_{na})}^{I(Z_{na})} = C - \omega_i \xi_{na} T_1 \quad (25)$$

From this relation, the slow time in  $T_1$  between two states of  $Z_{na}$  can be calculated. When the dynamics initiate on the right branch of the SIM, the SIM will be descended from  $Z_{na}(0)$  until  $Z_{na}^+$ . The duration of TET, called pumping time, is then:

$$\varepsilon T_{pmp} = \frac{1}{2\pi \xi_{na}} \left( I(Z_{na}(0)) - I(Z_{na}^+) \right) \quad (26)$$

with  $T_{pmp}$  relative to the period of the modal frequency, with  $T_{pmp} \frac{\omega_i}{2\pi}$  the time in seconds.

$Z_{na}^+$  is calculated from (18). But the value for  $Z_{na}(0)$  is ambiguous. As the pumping time is calculated from the slow flow dynamics and SIM (17), it is implicitly assumed that  $Z_0$  and  $Z_{na}$  are always on the SIM, even though the fast dynamics initiate on a line and not on the SIM.. To calculate  $T_{pmp}$ , the solution on the right branch of  $Z_{na}$  corresponding to  $Z_0(0)$  will be chosen, as visualized with the red diamond on Fig. 6a and Fig. 6b. With  $Z_{na}^+$  and  $Z_{na}(0)$  available, the pumping time (26) can be calculated without numerical integration of (17) or (1).

### 5.3 Pumping time damped main system

By allowing main system damping,  $\xi \neq 0$ , no separation of variables is possible in (24). Integrating both sides yields:

$$\begin{aligned} & (-\xi_{na} - \xi \xi_{na}^2 - \xi(1-\kappa)^2) T_1 \omega_i \\ & - \xi \omega_i \int_0^{T_1} \left( \frac{9}{16} Z_{na}^2 - (1-\kappa) \frac{3}{2} Z_{na} \right) \partial T_1 = I(Z_{na}) + C \end{aligned} \quad (27)$$

with  $C$  the constant of integration and  $I(Z_{na})$  (25). The slow time  $T_1$  between the two states  $Z_{na,1}$  and  $Z_{na,2}$  on the SIM is

$$\begin{aligned} & (-\xi_{na} - \xi \xi_{na}^2 - \xi(1-\kappa)^2) T_1 \omega_i \\ & - \xi \omega_i \int_0^{T_1} \left( \frac{9}{16} Z_{na}^2 - (1-\kappa) \frac{3}{2} Z_{na} \right) \partial T_1 \\ & = I(Z_{na,1}) - I(Z_{na,2}) \end{aligned} \quad (28)$$

The integral on the left-side equation is solvable if either the explicit function  $Z_{na}(T_1)$  is found, or a constant  $Z_{na}$  is assumed. Here it is opted for the latter as in [18] it was shown in simulations that  $Z_{na}$  is nearly constant during TET. This constant  $Z_{na}$ ,  $Z_{na}(t) = Z_{na,c}$ , is only assumed for the left side of equation (28) to solve the integral. Finally, the time between the two energy states, now chosen as  $Z_{na}(0)$  and  $Z_{na}^+$ , is:

$$\begin{aligned} & \left( -\xi_{na} - \xi \xi_{na}^2 - \xi(1-\kappa)^2 + \xi \left( \frac{9}{16} Z_{na,c}^2 - (1-\kappa) \frac{3}{2} Z_{na,c} \right) \right) \\ & \cdot T_{pump} 2\pi = I(Z_{na}(0)) - I(Z_{na}^+) \end{aligned} \quad (29)$$

from which the pumping time  $T_{pump}$  follows. Here, a  $Z_{na,c}$  is estimated as the average function value of  $Z_{na}$  of the equivalent system with no modal damping:

$$Z_{na,c} = \frac{2\pi}{\omega_i T_{pmp, \xi=0}} \int_0^{\omega_i T_{pmp, \xi=0} / 2\pi} Z_{na}(t) dt \quad (30)$$

In [18] the value of  $Z_{na,c}$  was determined by simulating the undamped slow flow dynamics and numerically calculating (30). Since this breaks the paradigm of expressing performance analytically without simulation,  $Z_{na,c}$  is analytically determined here.

When  $\xi = 0$ , then (24) can be written as

$$\begin{aligned} & \frac{1}{\omega_i \xi_{na}} \left( \frac{27}{32} Z_{na}^2 - 3(1-\kappa) Z_{na} + (1-\kappa)^2 + \xi_{na}^2 \right) \partial Z_{na} \\ & = -Z_{na} \partial T_1 \end{aligned} \quad (31)$$

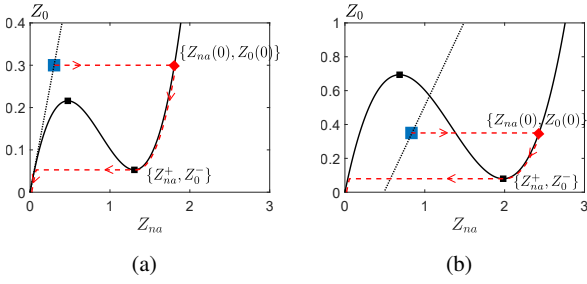


Fig. 6: Two SIMs, with one possible solution on the SIM, shown as a red diamond (a), and with three (b). To calculate the pumping time, the most right branch is chosen both times as the initial point on the SIM.

The integrated variable in (30) is changed to  $T_1$ , and together with (31):

$$\begin{aligned}
 Z_{na,c} &= \frac{1}{T_{1,p}} \int_0^{T_1} Z_{na}(T_{1,p}) dT_1 \\
 &= \frac{1}{\omega_i \xi_{na} T_{1,p}} \cdot \int_{Z_{na}^+}^{Z_{na}(0)} \left( \frac{27}{32} Z_{na}^2 - 3(1-\kappa)Z_{na} \right. \\
 &\quad \left. + (1-\kappa)^2 + \xi_{na}^2 \right) dZ_{na} \\
 &= \frac{1}{\omega_i \xi_{na} T_{1,p}} \cdot \left[ \frac{27}{96} Z_{na}^3 - \frac{3}{2}(1-\kappa)Z_{na}^2 + \right. \\
 &\quad \left. ((1-\kappa)^2 + \xi_{na}^2) Z_{na} \right]_{Z_{na}^+}^{Z_{na}(0)}
 \end{aligned} \tag{32}$$

with  $T_{1,p} = \frac{\varepsilon T_{pump} 2\pi}{\omega_i}$  the pumping time of the undamped main system expressed in the slow time scale  $T_1$ . With an expression for the average  $Z_{na}$  during TET in an undamped main system, (32), the pumping time for the equivalent system, yet with a damped main system, can be found with (29).

## 6 The chaotic threshold

### 6.1 Further reduced system

During chaotic inter-well vibrations, the BNES only has a marginal influence on the vibrations of the main system, as Figure 2b and Figure 2e illustrate. The main system's free vibrations closely resemble the free vibration without BNES, safe for a slow decay. The effect of the main system on the BNES can then be replaced by a ground excitation on the BNES. The ground excitation is the free vibration of the main system without NES. This technique has been used in [26] to numerically determine the energy threshold for TET for a NES with  $\kappa = 0$ , and was also used in [14]

to quantify chaotic vibrations of the BNES. Here, it will be used further on to tune the BNES. We retake (4) and assume an undamped main system:

$$\begin{cases} \ddot{x}_\ell + \omega_i^2 x_\ell + \varepsilon \ddot{x}_{na} = 0 \\ \varepsilon \ddot{x}_{na} + \varepsilon \lambda_{na} (\dot{x}_{na} - \dot{x}_\ell) + \varepsilon \Omega_3 \omega_i^4 (x_{na} - x_\ell)^3 \\ \quad + \varepsilon \kappa \omega_i^2 (x_{na} - x_\ell) = 0 \end{cases} \tag{33}$$

The first equation is solved under the assumption  $\varepsilon \ddot{x}_{na} \approx 0$ , valid if there is little interaction between the BNES and main system, which is the case during chaos. The solution for  $x_\ell$  is then  $x_\ell = x_\ell(0) \cos(\omega_i t) + \frac{\dot{x}_\ell(0)}{\omega_i} \sin(\omega_i t)$ . Reintroducing the relative absorber coordinate  $v$  to (33) yields:

$$\ddot{v} + \lambda_{na} \dot{v} + \Omega_3 \omega_i^4 v^3 + \kappa \omega_i^2 v = -X \sin(\omega_i t + \theta) \tag{34}$$

with

$$X = \sqrt{\omega_i^4 x_\ell(0)^2 + \omega_i^2 \dot{x}_\ell(0)^2} \quad \theta = \arctan\left(\frac{\omega_i x_\ell(0)}{\dot{x}_\ell(0)}\right)$$

By introducing the dimensionless time  $\tau = \omega_i t$  and coordinate  $v_d = \frac{v \omega_i^2}{X}$ , (34) becomes:

$$v_d'' + \xi_{na} v_d' + \Omega_3 (\omega_i^2 x_\ell(0)^2 + \dot{x}_\ell(0)^2) v_d^3 + \kappa v_d = -\sin(\tau + \theta) \tag{35}$$

with ' the derivative w.r.t.  $\tau$ . (35) reveals a forced Duffing oscillator which is known for its chaotic properties [27–29]. Although a Duffing oscillator can be analytically solved for some cases, namely the border between intra-well and chaos, there are no analytic techniques to find the threshold between chaotic regime and interwell vibrations. In the past numerical algorithms have been used to determine the so-called *Lyapunov exponent* of the Duffing oscillator, which is a measure of chaos [14, 28, 29]. Equation (35) reveals that the class of systems with equal  $\kappa$ ,  $\Omega_3$  and  $\xi_{na}$  and where the main system is impulsively excited,  $x_\ell(0) = 0$ ,  $\dot{x}_\ell(0) \neq 0$ , have the same dynamic behavior. The mass ratio  $\varepsilon$  also has no influence on (34).

### 6.2 Lyapunov exponent

The Lyapunov exponent (LE) is a quantifying measure for chaos in a dynamical system. It is the average exponential rate of divergence or decay of orbits initiating in nearby states [24]. For stable dissipative nonlinear systems, nearby states will either decay into a fixed point or limit cycle (non chaotic) or diverge into seemingly random and unpredictable dynamics (chaotic). For nonlinear ODEs, the LE is defined as the average exponential growth/decay of infinitesimal close states

$$\lambda_{LE} = \lim_{d(0) \rightarrow 0, t \rightarrow \infty} \frac{1}{t} \ln \left( \frac{d(t)}{d(0)} \right) \tag{36}$$

with  $d(t)$  the distance in phase space between a given orbit and a test orbit, initially starting infinitesimally close with initial distance  $d(0)$ . The LE depends on the chosen initial states and besides a few toy examples, are difficult to determine analytically. However, with the ODE given, the LE is numerically determined from (34) with the algorithm described in Wolf [30] with a Matlab implementation found on [31]. A first practical problem in calculating the LE is choosing the infinitesimally close states. In [30], an infinitesimal sphere is defined around the initial point with principle axis for each dimension of length  $p_i(0)$ . As time goes by this sphere stretches/contracts to an ellipsoid and its principle axis change length to  $p_i(t)$ . The change in length of these axis are then used to calculate the LE in (36). As numerically, infinitesimal distances are not possible, the algorithm of Wolf resort to the variational dynamics of the nonlinear system, approximated with the Jacobian, by definition describing the dynamics infinitely close to an initial condition. Another problem with (36) is that it requires an infinite time horizon. Therefore, the nonlinear dynamics are simulated for a time  $\tau$  starting from an initial condition  $x(0)$  resulting in  $x(\tau)$ , while the variational dynamics are simulated for orthonormal unit vectors  $e_i^{[1]}$  (a variation in each dimension on  $x(0)$ ) that are transformed by the Jacobian into  $v_i^{[1]}$ . The average exponential growth in the  $i$ -th dimension during  $\tau$  is  $\frac{1}{\tau} \ln(\|v_i^{[1]}\|)$ . The resulting  $v_i^{[1]}$ 's are re-orthonormalized to  $e_i^{[2]}$  in  $x(\tau)$  with the Gram-Smidt orthonormalization to prevent numerical errors because of exponential growth and decay, and to prevent that all vectors align according to the dominant eigenvalue. The nonlinear and variational dynamics are then simulated again over  $\tau$  starting from  $x(\tau)$  and  $e_i^{[2]}$  resulting in  $x(2\tau)$  and  $v_i^{[2]}$ . This process is repeated  $k$  times from which the LE can be calculated as:

$$\lambda_{LE} = \frac{1}{k\tau} \sum_{i=1}^k \ln\|v_i^{[i]}\| \quad (37)$$

The choice of  $\tau$  is not critical, but should be sufficiently small to prevent numerical errors if  $v_i$  decays or grows to fast, or their direction become indistinguishable because of dominant eigenvalues of the Jacobian. Often it is chosen as the expected period in the phase plane, here  $\tau = \frac{2\pi}{\omega_i}$ , the same period as the forcing term. Wolf's algorithm has been applied to the forced Duffing oscillator in [28] and was applied to a BNES in [14] to indicate its chaotic behavior. As the forced Duffing oscillator has two states and is linearly damped, it will have two negative LE for non-chaotic response and a positive and negative for chaotic response [30]. Further on, only the maximum LE will be considered, as this indicates chaos. No LE is calculated from the full dynamics (1) as the vibrations eventually decay even if the BNES initially vibrates chaotically and so will always yields negative

LE, stressing the need of the reduced 1DOF system. Furthermore, as not only the nonlinear system has to be calculated but also the variational dynamics, increasing the dimensions of the nonlinear system increases calculation time exponentially.

In [14], the forced Duffing oscillator is only used to predict chaotic behavior of the full system. Here, this prediction will be used to tune the BNES.

### 6.3 Numerical example of Lyapunov exponent

For the system in Section 3, the LE for initial speed  $\dot{x}(0)$  ranging from 0 to 0.1 m/s is numerically calculated for  $k = 1000$  and  $\tau = 2\pi$  in (37) and plotted on Figure 7 along with the absolute value of the average  $v$ , the relative absorber coordinate.  $|v_{mean}|$  indicates whether the BNES vibrates inter or intra-well, being (approximately) zero for TET and chaos and has the value of  $\sqrt{\frac{-k_{lin}}{k_{na}}} = 0.116$  for intra well vibrations. The system has a  $Z_0^+ = 0.4217$  while for  $\dot{x}(0) = 0.1$   $Z(0) = 0.2222$ . However, the threshold above which efficient TET ensues and below which there is a suboptimal chaotic response, is even lower. There is no chaos until  $\dot{x}(0) = 0.055$  m/s, as the  $LE < 0$ . Between  $\dot{x}(0) = 0.055$  and  $\dot{x}(0) = 0.02$  m/s there is chaos. The chaotic behavior halts below  $\dot{x}(0) = 0.02$  m/s, where the  $|v_{mean}| = 0.116$  indicates that the BNES vibrates intra-well. The dynamics (34) for  $\dot{x}(0) = 0.1$  m/s,  $\dot{x}(0) = 0.05$  m/s and  $\dot{x}(0) = 0.01$  m/s are plotted on a two-dimensional phase plane, Figure 8. The two fixed points are indicated by the red \*, and the separatrix of the Hamiltonion system is shown as red dash. It is called a separatrix as it separates distinct behaviors for the undamped and unforced system. When the dynamics start inside, it is confined within one of the lobes or wells and when started outside the trajectory orbits around the separatrix. The introduction of the forcing and damping introduces a third, chaotic behavior. These phase planes of the reduced system clearly visualizes the chaotic inter-well and intra-well oscillations, Figure 8b and Figure 8c

## 7 Chaos performance validation

### 7.1 Design

A NES and three BNES will be tuned for a damped SDOF mechanical system with  $m = 1$  kg,  $k = 1$  N/m,  $c = 0.002$  Ns/m and displacement  $x$ , which suffers from an impulsive load equivalent to  $\dot{x}(0) = 0.1$  m/s. The attached BNES has  $m_{na} = 0.02$  kg and  $c_{na} = 0.002$  Ns/m ( $\xi_{na} = 0.1$ ). The NES mass is chosen such that a small mass ratio is ensured,  $\varepsilon = 0.02$ . The choice of parameters also allows comparison to the single-mode simulation in [18, 32]. For  $\kappa = 0$ , the NES

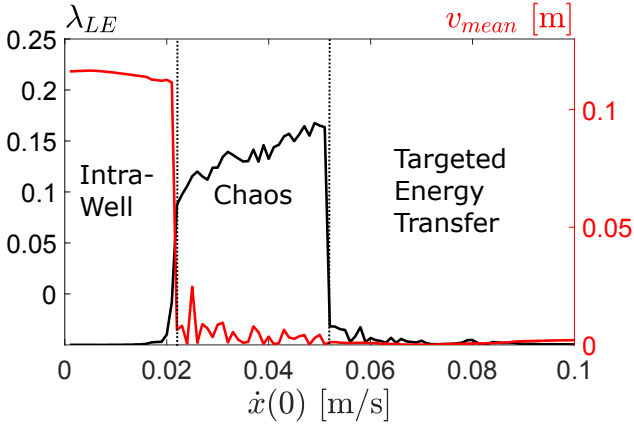


Fig. 7: The Lyapunov exponent and mean value obtained from numerical simulation of (34). The distinct behaviors is separated by a sudden change in LE and mean values

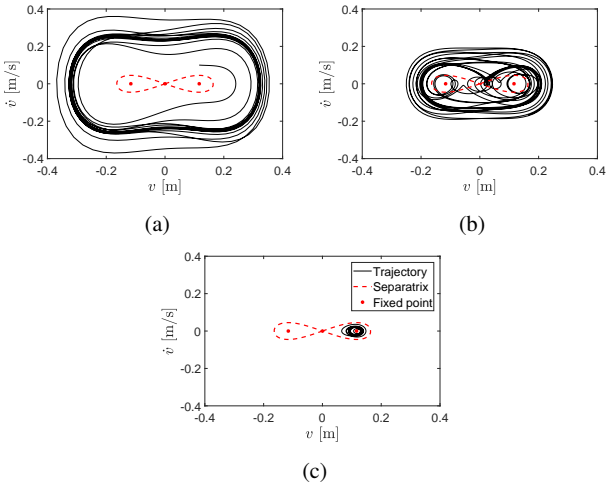


Fig. 8: The phase plane obtained from simulating the reduced Duffing oscillator (34), if there is TET (a), chaos (b) and intra-well vibrations (c).

is tuned with (20) yielding  $k_{na} = 0.444 \text{ N/m}^3$  ( $\Omega_3 = 22.2$ ). The BNES will not be tuned with (20), it will rather be tuned to avoid chaos by applying the novel tuning methodology. A chaos-performance graph is constructed for  $\xi_{na} = 0.1$  for a range of  $\Omega_3 = [0, 50]$  and  $\kappa = [0, -2]$  and shown on Fig. 9. The blue areas indicate a positive LE, or chaos, and the thick black line is a separator between inter-well and intra-well oscillations. Both are determined from numerical simulation of (34). Chaotic response seem to be independent of  $\kappa$  but rather dependent on how nonlinear ( $\Omega_3$ ) the BNES is. Then the algebraic performance is calculated with (29) and (22). The shades of pink represent the  $T_{pump}$  in  $s$  while the thin black line is a contour of constant  $E_{TET}$ . By choosing a  $\kappa$  and  $\Omega_3$  that avoids chaos and is in the inter-well region, a BNES is effectively tuned with an estimation of its per-

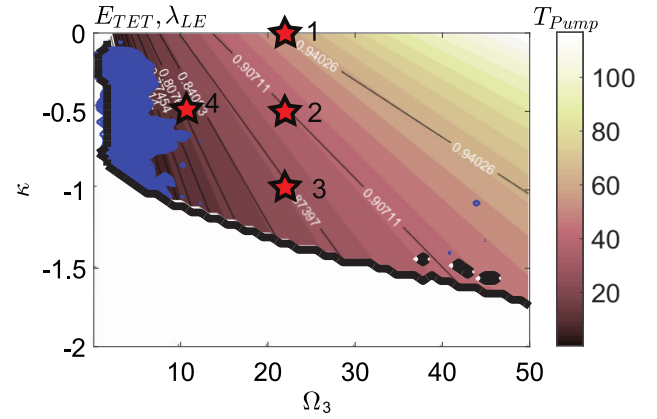


Fig. 9: For the given main system,  $\xi_{na} = 0.1$  and  $\dot{x}_0 = 0.1$ , positive LE exponent, (blue), indicating chaos,  $T_{pump}$  in shades of pink and  $E_{TET}$  as the thin black contour lines and white text. The thick black line separates inter and intra-well vibrations. Based on this graph, 4 NESs are tuned.

formance. The tuning methodology is not restricted to the choice of parameters made here. Therefore, at the end of this section, similar contour plots as Figure 9 are made for other choice of BNES damping and initial conditions.

Three BNESs will be simulated and compared to the NES with  $\kappa = 0$ , the choice of parameters corresponding with the stars on Figure 9. The pumping time and energy dissipation for the 4 NESs can be found on Table 1. Although 4 NESs are tuned assuming a fixed initial vibration energy,  $\dot{x}(0) = 0.1 \text{ m/s}$ , the initial energy will also be varied in the simulation to highlight the vastly different behavior of the NES for  $\kappa \geq 0$  and  $\kappa < 0$  and to showcase the BNES superiority in all cases.

|                                    | $E_{TET}$ | $Z_0^+$ | $T_{pmp}$ | $T_{pmp,sim}$ | % err |
|------------------------------------|-----------|---------|-----------|---------------|-------|
| 1) $\Omega_3 = 22$ $\kappa = 0.0$  | 0.202     | 0.94    | 60.2      | 68.0          | 11.4  |
| 2) $\Omega_3 = 22$ $\kappa = -0.5$ | 0.673     | 0.91    | 44.7      | 47.7          | 6.3   |
| 3) $\Omega_3 = 22$ $\kappa = -1.0$ | 1.589     | 0.90    | 35.6      | 34.1          | -4.4  |
| 4) $\Omega_3 = 13$ $\kappa = -0.5$ | 0.673     | 0.86    | 27.1      | 23.2          | -16.8 |

Table 1: Performance of the NESs tuned for an SDOF system

## 7.2 Mid energy simulation

NES 1, 2 and 3 on Table 1 were tuned for the initial condition of  $\dot{x}(0) = 0.1 \frac{m}{s}$ . This initial speed is applied here. All three NESs have a  $Z_0(0) \approx 0.22$ , which is above  $Z_0^+$  for NES 1, required to engage TET for  $\kappa \geq 0$ . For NES 2 and 3  $Z_0(0) < Z_0^+$  yet TET is still triggered, as expected from the relation between SIM and the initial line in Section 4.2.

The vibrations in the main system and absorber are respectively shown on Figure 10a and 10b. All three NESs engage in TET, as all three NESs vibrate with high amplitude. The duration of the TET, estimated beforehand with the pumping time on Table 1, is seen in the simulation as roughly the time the vibration in the main system stop mitigating at a fast rate. The NES with  $\kappa = 0$  is the slowest, while the two BNES are significantly faster. After TET, a residual amount of vibration energy remains. The amount of energy dissipation is also estimated and revealed that the BNES with  $\kappa = -1.0$  has the most residual energy which is confirmed by simulations. For  $\kappa = -0.5$ , the BNES is able to dissipate the residual energy quickly as it acts as a TMD when the NES is vibrating intra-well. To highlight that the previously derived slow flow dynamics are representative of the actual dynamics, the envelope of the simulation is calculated as  $E_{0,sim}(t) = \dot{u}^2(t) + \omega_f^2 u^2(t)$  and  $E_{na,sim}(t) = \dot{v}^2(t) + \omega_f^2 v^2(t)$  and compared to the simulation of the slow flow (17) on Figure 10c for  $E_0$  and Figure 10d for  $E_{na}$ . The pumping time is seen in the slow flow dynamics as either the time when the slope changes for  $E_0$  or the sudden jump in  $E_{na}$ . For  $E_0$ , the real dynamics follow the slow flow on average. There is less resemblance for  $E_{na}$ , as the real dynamics first need converge to the SIM, followed by a sudden jump, not immediately followed by the actual NES. Rather a smooth transition is made in the real dynamics, as the NES has an inertia.

The time for the actual energy envelope  $E_{0,sim}(t)$  to decay to the residual energy level  $E_{res} = 1 - E_{TET}$  is referred to pumping time of the actual simulation  $T_{pmp,sim}$  and is compared to  $T_{pmp}$  on Table 1. A good correspondence is found. For  $\kappa = 0$ ,  $T_{pmp}$  is an underestimation for the actual dissipation time while for the BNES it is more of an overestimation. On the phase plane of  $Z_0$  and  $Z_{na}$  the evolution of the slow flow, the envelope of the real dynamics are shown together with the SIMS on Figure 10e, 10f and 10g. While the slow dynamics initiate on the SIM, the actual dynamics do not and are attracted to the right branch of the SIM. Then the dynamics descend along the SIM until the local minimum, after which a jumps occurs.

The actual dynamics for  $\kappa = 0$  is initially above the maximum of the SIM  $Z_0(0) > Z_0^+$ , Figure 10e. For the BNESs,  $Z_0(0) < Z_0^+$ , yet still the actual dynamics are attracted to the right branch of the SIM. This is not possible when  $\kappa \geq 0$  if impulsive loading is considered, as discussed in section 4.2. Next, the initial vibration energy is lowered, such that  $Z_0(0) < Z_0^+$  also for the NES with  $\kappa = 0$ .

### 7.3 Lower initial energy simulation

By lowering the initial speed to  $\dot{x}(0) = 0.07$  m/s, the vibration mitigating behavior completely changes for all three NESs, Figure 11a and Figure 11b. For  $\kappa = 0$ ,  $Z_0(0) < Z_0^+$

which causes the dynamics to converge to the left branch of the SIM, Figure 11c. This confirms the condition that  $Z_0(0) > Z_0^+$  for  $\kappa \geq 0$ . Both BNESs vibrate chaotically, yet are able to dissipate the vibrations faster than NES # 1. When the NES vibrates chaotically, the fast dynamics are not confined to the SIM Figure 11d and Figure 11e, as the slow flow dynamics are not representative for chaotic vibrations.

### 7.4 Extremely Low initial energy simulation

By again lowering the initial speed now to  $\dot{x}(0) = 0.02$  m/s, the behavior of only the BNES changes, Figure 12a and Figure 12b. The NES with  $\kappa = 0$  still is vibrating suboptimally on the left branch of the SIM, Figure 12c. The SIM and slow flow dynamics are thus sufficient to describe this NES's behavior. The BNESs vibrate intra-well. While this also results in a slow energy dissipation for the BNES with  $\kappa = -1$ , the BNES with  $\kappa = -0.5$  is able to exponentially damp the vibrations because of its TMD feature during intra-well vibrations.

### 7.5 Influence of damping and initial energy on chaos & performance

To stress that the numerical calculation of the LE and the performance measures are of general purpose, the chaos-performance graph of Fig 9 is reconstructed for different BNES damping and different initial conditions. The pumping time is inversely proportional to the BNES damping  $\xi_{na}$  in the undamped main system case (26) and approximately in the damped main system case (29). To assess the influence on the chaotic response, the LE is numerically calculated and overlayed with the energy dissipation and pumping time for  $\xi_{na} = 0.05$  on Figure 13a and for  $\xi_{na} = 0.2$  on Figure 13b, respectively half and double the damping of the BNES in the previous section. The area of chaos increases as the damping increases. While the damping seems more or less inversely proportional to the pumping time, just increasing the damping to expedite the TET is not recommended as the area of chaos increases and the energy dissipation severely decreases.

If the initial speed is decreased, the area of chaos increases, see Figure 13c for  $\dot{x}(0) = 0.05$  while the pumping time decreases. This was already observed in the numerical simulation in Section 3. The decrease of initial energy means smaller part of the SIM needs to be descended, making TET shorter but also making chaos and intra-well oscillations appear sooner. By increasing the initial vibration energy, see Figure 13c for  $\dot{x}(0) = 0.15$ , the area of chaos severely decreases, while the pumping time increases.

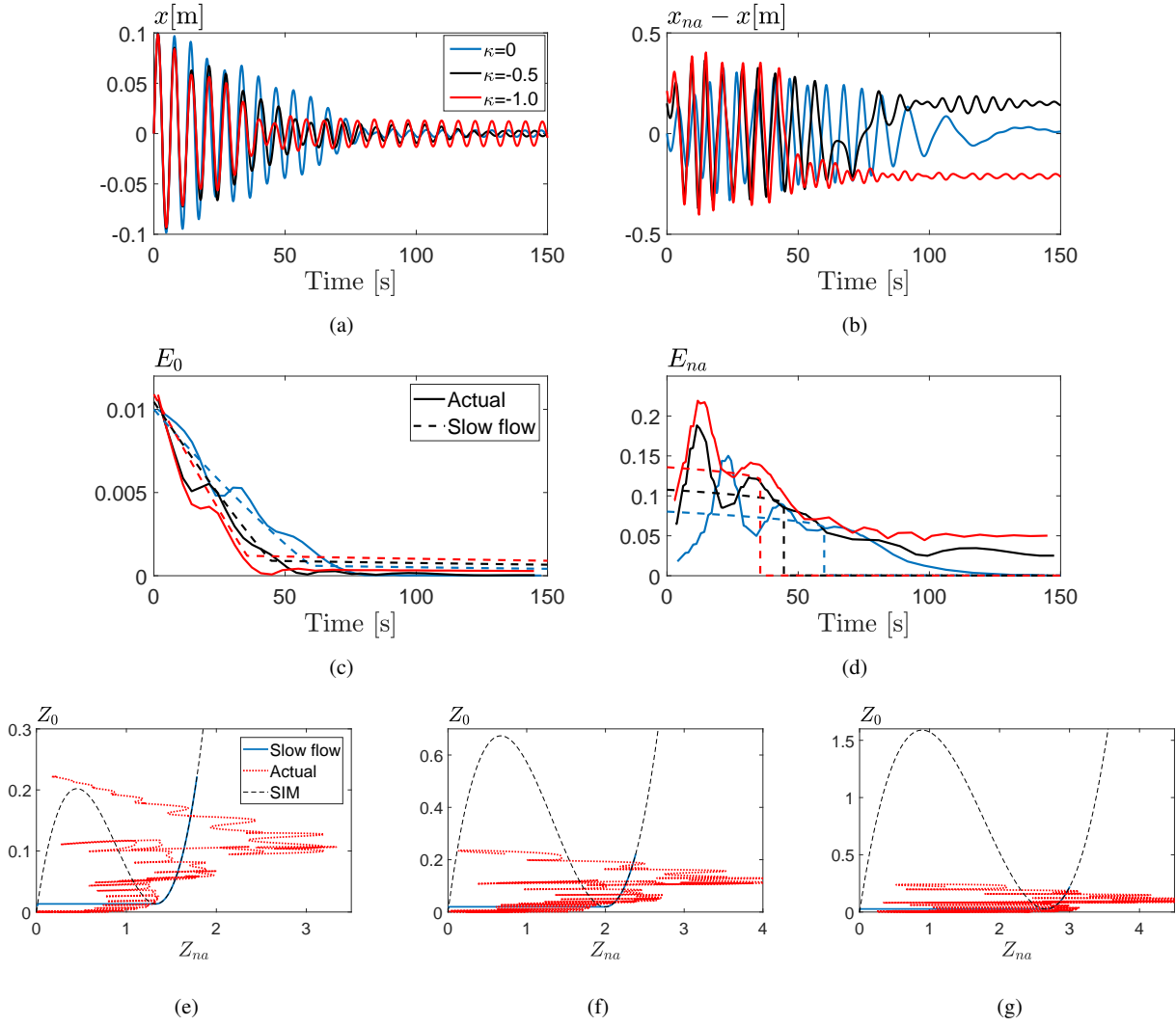


Fig. 10: Numerical simulation for  $\dot{x}(0) = 0.1$ , main system (a) and NES (b) vibration. Slow flow simulations vs actual dynamics (c) and (d). Phase plane of  $Z_{na}$  and  $Z_0$  with SIM, slow flow simulations and fast energies for NES # 1 (e), BNES # 2 (f) and more faster BNES # 3 (g)

The influence of mass ratio  $\varepsilon$  and assumed vibration mode  $\omega_i$  on chaos is not assessed here as these do not influence the reduced duffings oscillator (4), that is for the same range of  $\Omega_3$ ,  $\kappa$  and assuming impulsive excitation. The frequency  $\omega_i$  does however affect the physical parameters  $k_{na}$ ,  $c_{na}$  and  $k_{lin}$  for constant  $\Omega_3$ ,  $\kappa$  and  $\xi_{na}$ . Both  $\varepsilon$  and  $\omega_i$  are inversely proportional to the pumping time, (26) and (29) and do not affect the residual energy.

## 8 Robustness of BNES compared to TMD

In this section the performance and robustness of the BNES will be compared to the TMD. The TMD will be tuned by poleplacement such that its vibrations are critically damped, the fastest possible exponential decay. Let  $m_a$  be the TMD

mass,  $k_a$  the TMD stiffness and  $c_a$  the TMD damping. The response to impulsive load is critically damped if:

$$\frac{k_a}{m_a \omega_i^2} = \frac{1}{(1 + \varepsilon)^2} \quad \frac{c_a}{2\sqrt{m_a k_a}} = \sqrt{\frac{\varepsilon}{1 + \varepsilon}} \quad (38)$$

For  $\omega_i = 1$  and  $\varepsilon = 0.02$  and the same main system as in Section 7.1, the optimal TMD parameters are  $k_a = 0.0192$  and  $c_a = 0.0055$ . Observe the damping is almost triple than proposed for the BNES in Section 7.1. From the chaos-performance graph, Figure 9, an optimal BNES can be designed, indicated by 4 on the surface.  $\kappa$  is chosen as  $-0.5$  to swiftly dissipate the residual energy after TET.  $\Omega_3$  is chosen as 13.3, still outside of the chaotic region. Although the pumping time is about 27 s, Table 1, the residual energy is high. But as  $\kappa = -0.5$  the residual energy will be dissipated exponentially during intra-well vibrations. Comparing TMD and

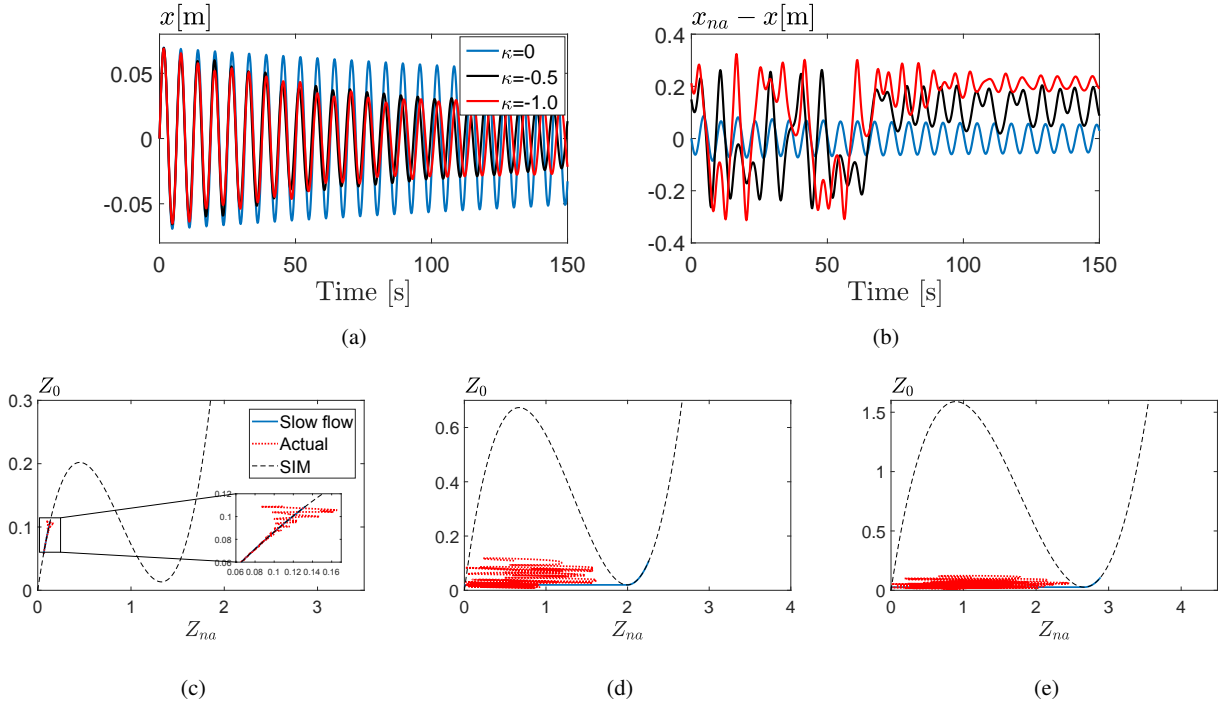


Fig. 11: Numerical simulation for  $\dot{x}(0) = 0.07$ , main system (a) and NES (b) vibration. Phase plane of  $Z_{na}$  and  $Z_0$  with SIM, slow flow simulations and fast energies for NES # 1 (e), BNES # 2 (f) and more faster BNES # 3 (g)

NES performance is not trivial, as there is no residual energy for a TMD. For the TMD the  $b\%$  settling time  $T_{set,b\%}$  is used to express the speed of dissipation. This is the time for the TMD to decay the vibrations of the main system to  $b\%$  of the initial amplitude.  $T_{set,b\%}$  is calculated with the eigenvalues of the compound linear system. Here,  $b\%$  is chosen as  $A_{res}\%$ , that is the fractional residual amplitude of the BNES in %, calculated with (23).  $T_{set,A_{res}\%}$  is then the time for the TMD to reduce the vibrations to the same level of residual amplitude of the BNES. For  $E_{TET} = 0.86$ , Table 1  $A_{res} = 0.37$  and for the TMD  $T_{set,37\%} = 28.8$ . The performance of the TMD and BNES seems quite similar. Both the BNES and TMD are simulated for  $\dot{x}(0) = 0.1 \frac{m}{s}$  with the main system's vibration and BNES/TMD vibration on respectively Figure 14a and 14b. Initially, the BNES dissipates at a faster rate than the TMD. However, after the pumping time, the BNES performance deteriorates while the TMD ensures an optimal exponential decay at all times. A BNES, and NESs in general, are however better equipped against detuning. The same BNES and TMD are simulated again, but now the main system's frequency is decreased to  $\omega_i = 0.75$ , Figure 14c and Figure 14d. The BNES is about two times slower than if  $\omega_i = 1$  but the TMD performance is just abysmal. In [33], a robust tuning procedure for a TMD was proposed for uncertain main system under harmonic forcing but is applied here for transient vibrations. It minimizes the worst case response in a given uncertainty range

of the natural frequency  $\omega_i$ . Given a range of  $\omega_i \in [0.75, 1]$ , the robust TMD has a stiffness  $k_a = 0.0126$  and almost doubled  $c_a = 0.0089$ . It is then not optimal for  $\omega_i = 1$  in the poleplacement sense as the vibration then decay supercritically but its performance suffers less from detuning. The 'optimal' TMD, the robust TMD and the BNES are now compared for a range  $\omega_i \in [0.65, 1]$ . For this range,  $E_{TET}$  and  $T_{pmp}$  are calculated for the BNES and the corresponding  $T_{set,A_{res}\%}$  is determined for both TMD's. The BNES energy dissipation does increase, Figure 14e, at the cost of increased pumping time, 64 s for  $\omega_i = 0.75$  and even 95 s for  $\omega_i = 0.65$ , Figure 14f. The optimal TMD's performance degrade significantly more with  $T_{set}$  going from 28.8 s to 315 s for  $\omega_i = 0.75$  and even to 902 s for  $\omega_i = 0.65$ . The robust TMD, suboptimal for  $\omega_i = 1$  with  $T_{set} = 72.35$  s eventually performs better for increased detuning than the optimal TMD, only increasing to 98 s for  $\omega_i = 0.75$ . Outside the assumed range the performance deteriorates to 216 s for  $\omega_i = 0.65$ . At the central frequency in the range  $[0.75, 1]$ ,  $\omega_i = 0.875$ , the robust TMD is actually optimal at  $T_{set} = 68$  s, with the corresponding pumping time of the BNES at 41 s. In conclusion, a BNES is more robust against a uncertain mechanical system than both the optimal TMD and a robustly designed TMD.

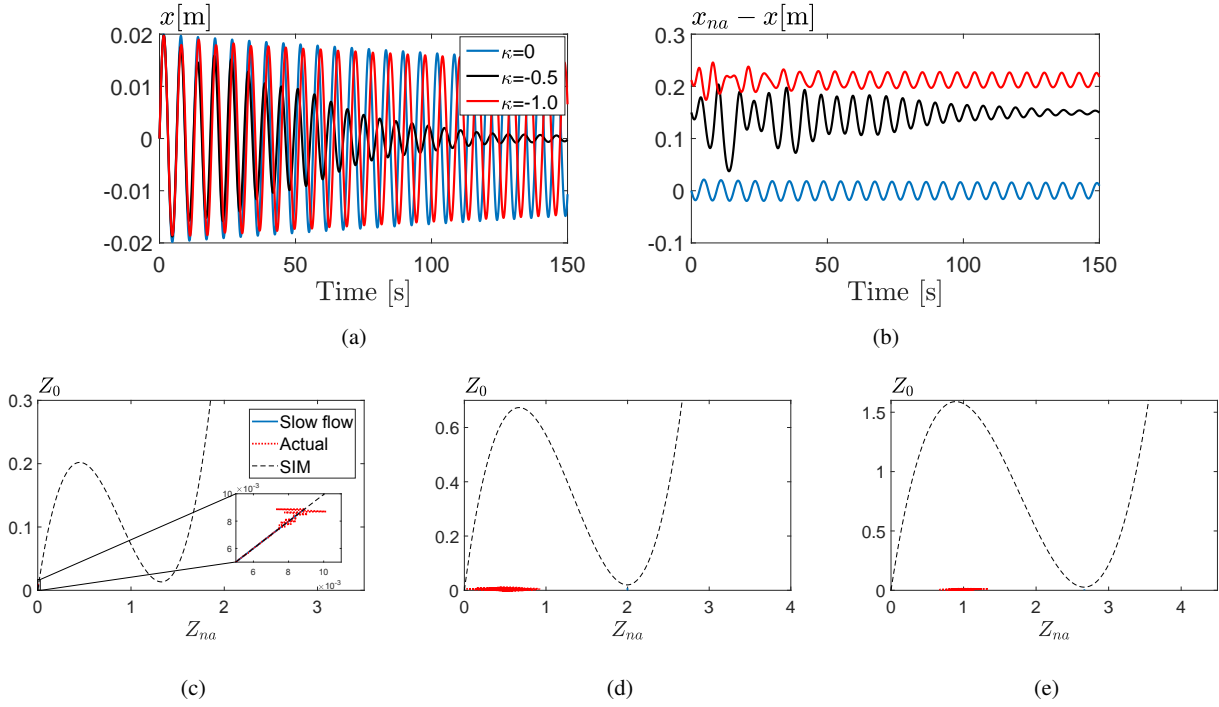


Fig. 12: Numerical simulation for  $\dot{x}(0) = 0.02$ , main system (a) and NES (b) vibration and SIMs (c-e)

| NES | $T_{pmp, \omega_i=1} \frac{\omega_i}{2\pi}$ [s] | $T_{pmp, \omega_i=0.75} \frac{\omega_i}{2\pi}$ [s] | $T_{pmp, \omega_i=0.65} \frac{\omega_i}{2\pi}$ [s] |
|-----|---|--|--|
| 4   | 27.1  | 64.45  | 95   |
| TMD | $T_{set, \omega_i=1}$ [s]                       | $T_{set, \omega_i=0.75}$ [s]                       | $T_{set, \omega_i=0.65}$ [s]                       |
| 1   | 28.8  | 315  | 902  |
| 2   | 72.35   | 98   | 216  |

Table 2: Performance of the NESs tuned for an SDOF system

## 9 Conclusion

This research presented a complete study of tuning and performance of a bi-stable NES in damping transient single-mode vibrations. While there were quite some similarities found between a bi-stable NES (BNES) and a non bi-stable NES for high and mid energy level vibrations, as for both the performant targeted energy transfer (TET) occurs, their behavior completely diverges for the lower energy levels. Below some initial energy threshold value, the BNES vibrates chaotically and for even lower vibration energy the BNES vibrates intra-well, closely to one of its stable equilibrium points. For both operations the mitigation of vibrations was poorly. As the most performant vibration mitigation happens during TET, a numerical method was designed in this study to find the threshold between chaotic vibration and TET. By simplifying the compound system of mechanical system and NES to a forced Duffing oscillator, the Lyapunov exponent (LE) was numerically calculated from this Duffing oscillator. The BNES should be tuned such that

the LE of the equivalent Duffing oscillator indicated non-chaotic behavior. By avoiding this chaos, a BNES could be tuned that was superior both to other NESs and tuned-mass-dampers (TMD). The performance of the BNES is assessed with the algebraic performance measures pumping time and energy dissipation or residual energy. These allow the performance to be estimated without simulations. The pumping time estimates how long TET takes while the energy dissipation estimates how much of the initial vibration energy is dissipated during TET, with the remaining residual energy damped very slowly. Both measures predicted a superior performing BNES, which was confirmed in actual numerical simulation. A BNES does however lead to increased residual vibrations after TET. The negative linear part of the BNES could be chosen such that the BNES acts as a TMD during intra-well vibration. This way, a BNES is able to dissipate vibrations quickly both during TET, and the residual energy after TET during intra-well vibrations. This is not possible for other NESs, where increased pumping time always leads to more residual vibrations. The influence of the BNES damping and initial vibration energy on both chaotic behavior and performance was determined. While an increase in damping did hasten the pumping time, sub-optimal chaotic vibrations occurred for a much wider range of NES parameters. The same holds for a decrease in the initial vibration energy. In both cases the residual vibration energy also increased. As with other NESs, there is a trade-off in speed and the amount of energy dissipated, and additionally for



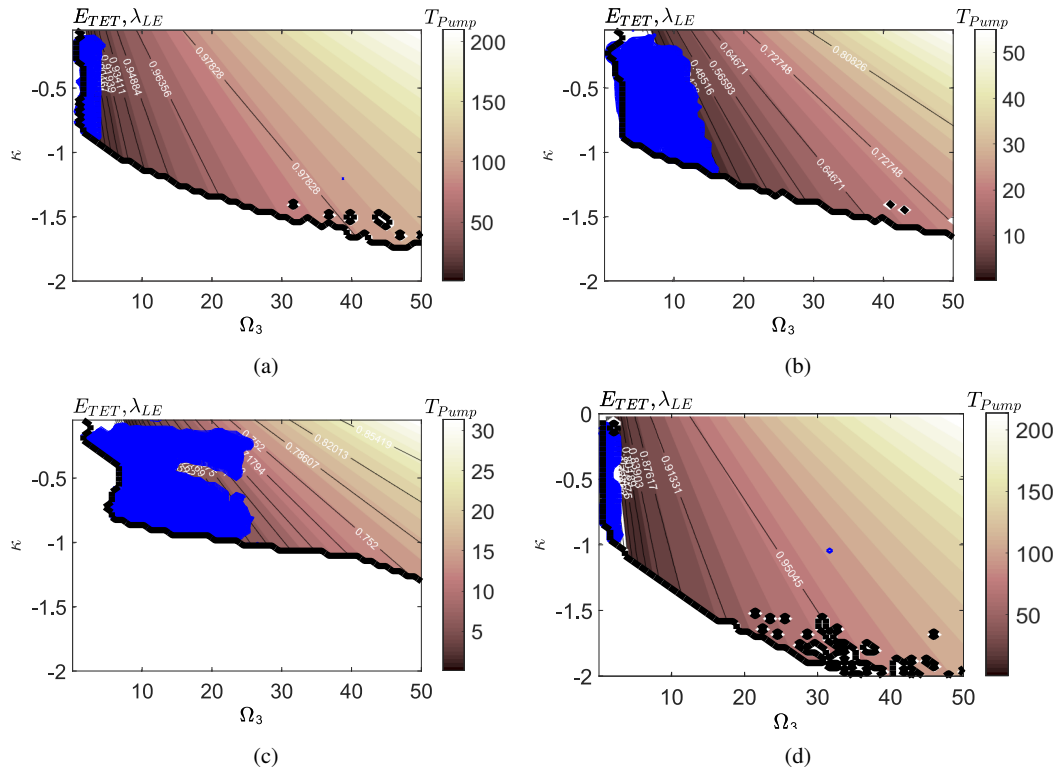


Fig. 13: The influence of damping on chaos and performance of the BNES, (a) for  $\xi_{na} = 0.05$  and (b)  $\xi_{na} = 0.2$ , and influence of the initial energy,  $\dot{x}(0) = 0.05$  (c) and  $\dot{x}(0) = 0.15$  (d) with  $\xi_{na} = 0.1$

the BNES, a greater chance of chaos. The performance of the BNES for an uncertain main system was compared to the TMD. The BNES was found to be far more robust, even when considering a robust TMD design.

### Conflict of Interest

The authors declare that they have no conflict of interest.

### References

1. A. F. Vakakis, O. V. Gendelman, L. A. Bergman, M. D. McFarland, G. Kerschen, Y. S. Lee, *Nonlinear Targeted Energy Transfer in Mechanical and Structural Systems*, Springer Netherlands, 2009.
2. F. Petit, M. Loccufer, D. Aeyels, Feasibility of nonlinear absorbers for transient vibration reduction, in: *Proceedings of ISMA 2010: international conference on noise and vibration engineering*, 2010, pp. 1219–1233.
3. Y. S. Lee, G. Kerschen, A. F. Vakakis, P. Panagopoulos, L. A. Bergman, M. D. McFarland, Complicated dynamics of a linear oscillator with a light, essentially nonlinear attachment, *Physica D: Nonlinear Phenomena* 204 (2005) 41–69.
4. G. Kerschen, Y. S. Lee, A. F. Vakakis, D. M. McFarland, L. A. Bergman, Irreversible passive energy transfer in coupled oscillators with essential nonlinearity, *SIAM Journal on Applied Mathematics* 66 (2) (2005) 648–679.
5. A. Tripathi, P. Grover, T. Kalmár-Nagy, On optimal performance of nonlinear energy sinks in multiple-degree-of-freedom systems, *Journal of Sound and Vibration* 388 (2017) 272–297.
6. D. Qiu, T. Li, S. Seguy, M. Paredes, Efficient targeted energy transfer of bistable nonlinear energy sink: application to optimal design, *Nonlinear Dynamics* (2018) 1–19.
7. M. A. AL-Shudeifat, Highly efficient nonlinear energy sink, *Nonlinear Dynamics* 76 (4) (2014) 1905–1920.
8. S. Chiacchiari, F. Romeo, D. M. McFarland, L. A. Bergman, A. F. Vakakis, Vibration energy harvesting from impulsive excitations via a bistable nonlinear attachment, *International Journal of Non-Linear Mechanics* 94 (2017) 84–97.
9. S. Chiacchiari, F. Romeo, D. M. McFarland, L. A. Bergman, A. F. Vakakis, Vibration energy harvesting from impulsive excitations via a bistable nonlinear attachment: experimental study, *Mechanical Systems and Signal Processing* 125 (2019) 185–201.
10. M. Farid, O. V. Gendelman, Tuned pendulum as nonlinear energy sink for broad energy range, *Journal of Vibration and Control* 23 (3) (2017) 373–388.
11. X. Fang, J. Wen, J. Yin, D. Yu, Highly efficient continuous bistable nonlinear energy sink composed of a cantilever beam with partial constrained layer damping, *Nonlinear Dynamics* 87 (4) (2017) 2677–2695.
12. E. Gourdon, C.-H. Lamarque, Energy pumping with various nonlinear structures: numerical evidences, *Nonlinear dynamics* 40 (3) (2005) 281–307.
13. O. V. Gendelman, C.-H. Lamarque, Dynamics of linear oscillator coupled to strongly nonlinear attachment with multiple states of equilibrium, *Chaos, Solitons & Fractals* 24 (2) (2005) 501–509.
14. F. Romeo, L. Manevitch, L. Bergman, A. Vakakis, Transient and chaotic low-energy transfers in a system with bistable nonlinearity,

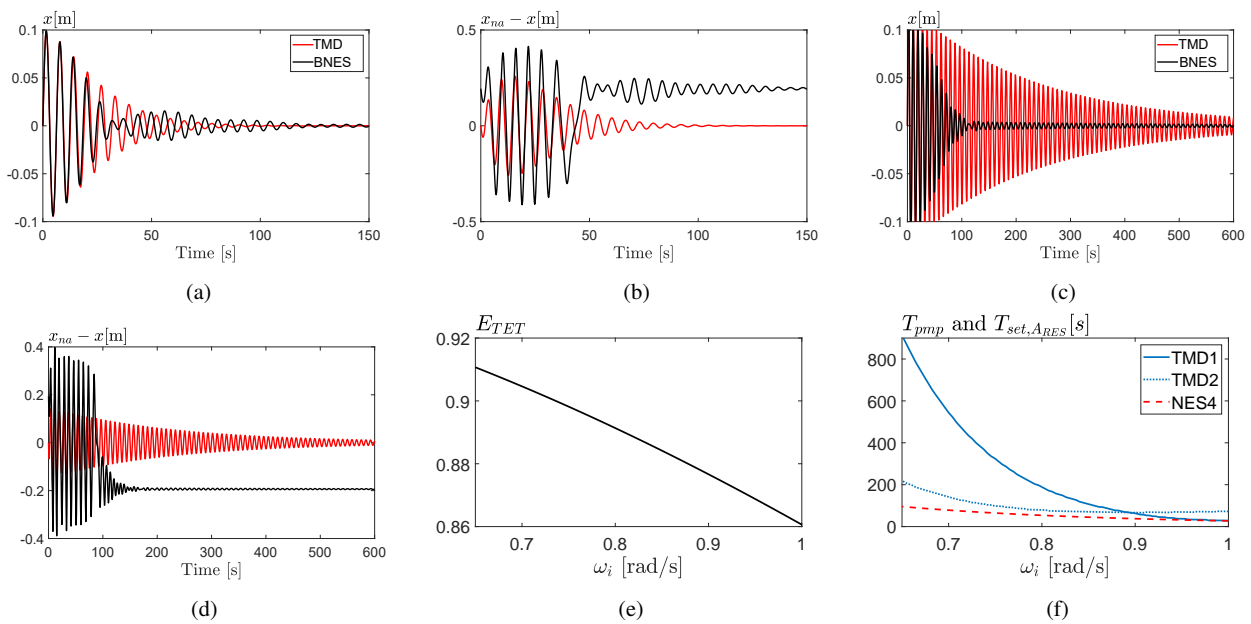


Fig. 14: The performance of a BNES compared to a TMD, main system vibrations (a) and NES vibrations (b) tuned for  $\omega_i = 1$ , when detuned with  $\omega_i = 0.75$  (c)(d). The energy dissipation of the BNES when detuning (e) and the corresponding pumping time and settling time (f)

- Chaos: An Interdisciplinary Journal of Nonlinear Science 25 (5) (2015) 053109.
15. G. Habib, F. Romeo, The tuned bistable nonlinear energy sink, *Nonlinear Dynamics* 89 (1) (2017) 179–196. doi:10.1007/s11071-017-3444-y.
  16. B. Vaurigaud, A. T. Savadkoobi, C.-H. Lamarque, Targeted energy transfer with parallel nonlinear energy sinks. part i: design theory and numerical results, *Nonlinear dynamics* 66 (4) (2011) 763–780.
  17. T. A. Nguyen, S. Pernot, Design criteria for optimally tuned nonlinear energy sinks part I: transient regime, *Nonlinear Dynamics* 69 (1-2) (2012) 1–19.
  18. K. Dekemele, R. De Keyser, M. Loccufer, Performance measures for targeted energy transfer and resonance capture cascading in nonlinear energy sinks, *Nonlinear Dynamics* (2018) 1–26 doi: 10.1007/s11071-018-4190-5.
  19. K. Avramov, Y. V. Mikhlin, Snap-through truss as a vibration absorber, *Modal Analysis* 10 (2) (2004) 291–308.
  20. F. Romeo, G. Sigalov, L. A. Bergman, A. F. Vakakis, Dynamics of a linear oscillator coupled to a bistable light attachment: numerical study, *Journal of Computational and Nonlinear Dynamics* 10 (1) (2015) 011007. doi:10.1115/1.4027224.
  21. L. Manevitch, G. Sigalov, F. Romeo, L. Bergman, A. Vakakis, Dynamics of a linear oscillator coupled to a bistable light attachment: analytical study, *Journal of Applied Mechanics* 81 (4) (2014) 041011. doi:10.1115/1.4025150.
  22. S. Benacchio, A. Malher, J. Boisson, C. Touzé, Design of a magnetic vibration absorber with tunable stiffnesses, *Nonlinear Dynamics* 85 (2) (2016) 893–911.
  23. S. L. Feudo, C. Touzé, J. Boisson, G. Cumunel, Nonlinear magnetic vibration absorber for passive control of a multi-storey structure, *Journal of Sound and Vibration* 438 (2019) 33–53.
  24. S. H. Strogatz, *Nonlinear dynamics and chaos: with applications to physics, biology, chemistry, and engineering*, Hachette UK, 2014.
  25. O. V. Gendelman, Bifurcations of nonlinear normal modes of linear oscillator with strongly nonlinear damped attachment, *Nonlinear Dynamics* 37 (2) (2004) 115–128.
  26. F. Petit, M. Loccufer, D. Aeyels, The energy thresholds of nonlinear vibration absorbers, *Nonlinear dynamics* 74 (3) (2013) 755–767.
  27. I. Kovacic, M. J. Brennan, *The Duffing equation: nonlinear oscillators and their behaviour*, John Wiley & Sons, 2011.
  28. J. Wei, G. Leng, Lyapunov exponent and chaos of duffing's equation perturbed by white noise, *Applied Mathematics and Computation* 88 (1) (1997) 77–93.
  29. A. R. Zeni, J. A. Gallas, Lyapunov exponents for a duffing oscillator, *Physica D: Nonlinear Phenomena* 89 (1-2) (1995) 71–82.
  30. A. Wolf, J. B. Swift, H. L. Swinney, J. A. Vastano, Determining lyapunov exponents from a time series, *Physica D: Nonlinear Phenomena* 16 (3) (1985) 285–317.
  31. V. Govorukhin, Calculation lyapunov exponents for ode, <https://nl.mathworks.com/matlabcentral/fileexchange/4628-calculation-lyapunov-exponents-for-ode> (2004).
  32. K. Dekemele, P. Van Torre, M. Loccufer, Optimization of multimodal targeted energy transfer performance of nonlinear passive vibration absorbers, in: *Proceedings of ISMA 2018: international conference on noise and vibration engineering*, 2018.
  33. L. Dell'Elce, E. Gourc, G. Kerschen, A robust equal-peak method for uncertain mechanical systems, *Journal of Sound and Vibration* 414 (2018) 97–109.